Energy & Environmental Science

REVIEW

View Article Online
View Journal | View Issue

Cite this: *Energy Environ. Sci.*, 2019, **12**, 518

From scalable solution fabrication of perovskite films towards commercialization of solar cells

Fei Huang,†[a] Mengjie Li,†[a] Peter Siffalovic,[b] Guozhong Cao *[c] and Jianjun Tian *[a]

Organic–inorganic halide perovskite solar cells (PSCs) have achieved amazing progress in terms of power conversion efficiency (PCE), rising from 3.8% to over 23.3%. Owing to perovskites' low nucleation and crystallization activation energy (56.6–97.3 kJ mol^{-1}), a range of low temperature and large-scale solution fabrication processes have been actively investigated for potential commercialization. Although many excellent research institutes and enterprises have emerged to advance commercialization of PSCs, the performance of devices which have large areas still lag much farther behind those of smaller lab scales. The performances of PSCs are predominantly determined by the quality of the perovskite film, which in turn, is controlled by the fabrication process. A comprehensive and in-depth understanding of the nucleation and growth process during perovskite crystallization is imperative for the further advancement of large-scale manufacturing of high quality perovskite films. This review summarizes recent advances in the commercialization of the PSCs market, and critically reviews promising large-scale solution manufacturing methods combined with their physical properties and relevant challenges with the crystallization thermodynamics and kinetics of perovskites. The hurdles and challenges of commercialization and possible approaches and solutions are discussed.

Received 15th October 2018,
Accepted 30th November 2018

DOI: 10.1039/c8ee03025a

rsc.li/ees

Broader context

Organic–inorganic halide perovskites possess a combination of excellent properties, such as low cost and easy solution synthesis. Perovskite solar cells (PSCs) have achieved great progress in the past decade with their power conversion efficiency (PCE) reaching 23.3% in laboratory scale, making them the most promising next generation photovoltaic. Other applications of perovskite devices for sensing and light emitting are also under intensive study and making rapid progresses. However, successful commercialization of PSCs and other perovskite devices are all critically dependent on the ability of cost-effective scalable fabrication of large sized high quality perovskite films or crystals, most presumably through solution processes. This review presents a comprehensive coverage of studies on the scalable solution fabrication of perovskite films with both information on technical approaches and the fundamental rationale and mechanisms involved. More specifically, an in-depth understanding of the thermodynamics and kinetics of perovskite's nucleation and crystallization are elaborated on as a basic foundation for the development of scalable fabrication methods for high quality perovskite films in support of commercialization. Other technical and environmental hurdles and challenges for commercialization of PSCs, such as low PCE for large area (>10 cm^2), module cost, long-term stability, and toxicity of lead and solvents have also been discussed.

1. Introduction

Organic–inorganic halide perovskites (such as $CH_3NH_3PbI_3$) solar cells (PSCs) have risen to stardom owing to their intrinsic broad and strong optical absorption, high charge carrier mobility, low exciton binding energy, and long free carrier diffusion length as well as their cost-effective and easy solution manufacturing.[1,2] Miyasaka and his colleagues[3] first studied an organic–inorganic halide perovskite as a sensitizer for solar cells and their work immediately simulated a "gold rush" in the research field of solar cell materials and devices. PSCs have achieved remarkable progress with power conversion efficiency (PCE), rising from 3.8% in 2009 reported by Miyasaka's group to 23.3% in 2018 reported by You's group for small sized (<1 cm^2) devices.[3,4] Recently, many efforts have been focused on large-area perovskite modules and they have been making great progress in performance.[5–7] PSCs have become a strong competitor in the photovoltaic field, rivaling the widely successful silicon-based solar cells, the mature thin-film cadmium

[a] *Institute for Advanced Materials and Technology, University of Science and Technology Beijing, 100083, China. E-mail: tianjianjun@mater.ustb.edu.cn*
[b] *Institute of Physics, Slovak Academy of Sciences, Bratislava, 84511, Slovakia*
[c] *Department of Materials Science and Engineering, University of Washington, Seattle, WA, 98195-2120, USA. E-mail: gzcao@u.washington.edu*
† Fei Huang and Mengjie Li contributed equally to this work and should be considered co-first authors.

telluride (CdTe), and copper indium gallium selenide (CIGS) solar cells.[8,9] This rapid progress in achieving excellent PCEs is largely due to optimizing the device's architecture, modulate hole and electron transfer, interface engineering, and fabrication processes with high quality perovskite films.[10–16] This progress has promptly motivated the photovoltaic communities' efforts to commercialize PSCs.

The perovskite layer is at the core of PSCs, whose quality directly determines a device's performance. According to *in situ* X-ray scattering studies, the nucleation and crystallization activation energy of a perovskite (56.6–97.3 kJ mol^{-1}) is much lower than that of amorphous silicon (280–470 kJ mol^{-1}).[17,18] A low crystallization energy barrier allows the perovskite films to be readily prepared by a variety of low-temperature large-scale fabrication processes including ink-jet printing, doctor-blading, and roll-to-roll print, which sets up a bridge between academic research and industrial applications.[19–21] In recent years, with improvements in fabrication technology and processes, the commercialization of PSCs has become an unstoppable trend and many excellent research institutions and companies have emerged worldwide and offered promising hope for the PSCs market. The main PSCs research institutions and companies and their major accomplishments are listed in Table 1. To accelerate the commercialization of PSCs, Oxford Photovoltaics

Fei Huang

Fei Huang is currently a lecturer as well as research fellow in the Institute for Advanced Materials Technology at the University of Science and Technology Beijing. She studied as a visiting student at the University of Washington (Seattle) from 2014 to 2016. She earned a PhD degree from Donghua University in 2017. She joined the Laboratory of Optoelectronic Materials and Devices at USTB in 2017. Her recent research mainly focuses on quantum dot sensitized solar cells and perovskite solar cells.

Mengjie Li

Mengjie Li earned a master's degree from the University of Science and Technology Beijing in 2018 supervised by Prof. Jianjun Tian. Her post-graduate study was focused on perovskite solar cells in the Laboratory of Optoelectronic Materials and Devices. She is currently working at Hanergy Thin Film Power Group, researching CIGS solar cells.

Peter Siffalovic

Peter Siffalovic is a core researcher at the Institute of Physics, Slovak Academy of Sciences. He completed his PhD at Bielefeld University (Germany) in 2002 working on femtosecond time-resolved photoelectron spectroscopy. His research focuses on a deeper understanding of self-assembly and crystallization kinetics of a wide range of materials including perovskites for solar cell research by means of wide- and small-angle X-ray scattering.

Guozhong Cao

Guozhong Cao is Boeing-Steiner Professor of materials science and engineering, chemical engineering, and adjunct professor of mechanical engineering at the University of Washington (Seattle). His current research is focused on chemical processing of nanomaterials for energy-related applications including solar cells, rechargeable batteries, supercapacitors, and hydrogen storage. He has published over 400 peer-reviewed papers with more than 33 000 citations.

Jianjun Tian

Jianjun Tian is a professor in the Institute for Advanced Materials and Technology, University of Science and Technology Beijing (USTB). He received his PhD in USTB in 2007 and built the Laboratory of Optoelectronic Materials and Devices at USTB in 2016. His current research focuses on optoelectronic materials and devices, regarding quantum dots/perovskites and their application in solar cells, light emitting and photodetectors. He has published over 80 peer-reviewed papers with more than 2500 citations.

Table 1 PSCs research institutions and companies and their major progresses[23,24,26–29]

Co. name	Country	Major progress
Oxford photovoltaics, Ltd	United Kingdom	A PCE of 27.3% for perovskite/silicon tandem cell
Solaronix	Switzerland	A PCE of 12% for 500 cm^2 module
EPFL	Switzerland	A PCE of 11.2% for 100 cm^2 solar panels remained stable for over a year
Greatcell Solar, Ltd	Australia	Focused on the solar enablement of two principal substrates: glass and steel
Toshiba	Japan	A PCE of 10.5% for a 25 cm^2 flexible module
Microquanta Semiconductor Co., Ltd	China	A PCE of 17.9% for a 227 cm^2 module

Ltd (Oxford PV), with technology from Snaith's lab in the Physics Department of Oxford University, has been working on the commercialization of perovskite technology for several years. They aimed at bringing perovskite/silicon tandem cells to the market and establishing module fabrication lines, also through collaboration with the leading German research center (Helmholtz-Zentrum Berlin (HZB)) on energy materials to accelerate the introduction of PSCs technology into silicon cell manufacturing lines.[22] Recently, they announced that a certified PCE of their perovskite/silicon tandem solar cell has reached a new record of 27.3%.[23] Solaronix in Switzerland is working on scalable fabrications of stable and high performance large-area all-print perovskite solar cell modules, and they produced 500 cm^2 perovskite solar cell modules with simple printing techniques and produced a 12% PCE in July 2016.[24] In 2017, Solaronix announced that a PCE of its carbon materials-based monolithic perovskite solar cells at lab scale reached more than 14% with low materials cost and high stability.[25] Also in 2017, in collaboration with Grätzel's group and Solaronix, the Swiss Federal Institute of Technology in Lausanne (EPFL) assembled 2D/3D hybrid PSC, fully printed 100 cm^2 solar panels with a PCE of 11.2% which were stable for over a year.[26] The Australian firm, Greatcell Solar Ltd, formerly Dyesol, was just awarded €500 000 in a European Union Horizon 2020 project[27] to develop advanced technologies for high efficiency, long lifetime PSCs and for a Building Integrated PV (BIPV). Toshiba produced 5 cm × 5 cm flexible multi-cell mini-modules with the highest PCE of 10.5% using a new printing process in Sep. 2017.[28] They aimed at driving costs down for flexible solar panels, particularly for BIPV applications. Microquanta Co., Ltd in Hangzhou, China, has refreshed the world's record efficiency of a perovskite solar module three times during 2017, with the most recent PCE of 17.9% in its solar module with an illumination area of 17.277 cm^2.[29] Although great efforts have been made with technique innovations for commercialization of PSCs, many challenges still remain. With relatively low PCEs, the lack of mature large-scale manufacturing technology, long-term stability, and toxicity issues are considered as the main barriers to wide spread commercialization[30–33] while high PCEs can be obtained only with small sized devices (typically between 0.03–0.2 cm^2), which are too small for commercialization.[9] One of the critical challenges is how to develop and improve the manufacturing process in order to fabricate the large-area devices (1 cm^2 or even larger) without a considerable reduction of PCE from that of small area devices.

In the past decade, great efforts have been made in the PSC research field and many excellent works have been published on topics such as fundamentals, perovskite fabrication, architecture optimization, surface passivation, stability, toxicity, hole transfer, and electron transfer materials.[2,11,34–42] These have resulted in significant advancements as reflected with the rapid increase in PCEs and large number of high quality publications realizing that scalable fabrication is one of the most important steps towards full PSC commercialization. Many excellent and authoritative review papers have been published to summarize the advances of up-scaling of PSC.[43–49] For example, Rong *et al.*[43] made a comparison of different fabrication methods of large-scale fabrication of PSCs and suggested that screen printing and slot-die coating may be the most promising methods. Jung *et al.*[44] reviewed the progress in scalable coating and roll-to-roll compatible printing processes as well as related morphology control methods for PSCs. However, a systematic and comprehensive understanding of the nucleation/crystallization mechanism as well as its' correlation with scalable fabrication techniques are still limited. Considering that large-scale manufacturing of perovskite films is mainly based on solution processes, an in-depth understanding of nucleation and growth processes of perovskite crystals is essential to obtain a high-quality perovskite film, which is directly linked with the performance of PSCs. This review starts with the mechanism of nucleation and growth of perovskite thin films and puts emphasis on the review of a variety of promising large-scale fabrication processes, including possible solutions, which may enable the transition of lab-scale devices towards their commercialization. Major hurdles of current PSCs, including long-term stability, toxicity, and cost are discussed, and some conceivable solutions to overcome barriers on the way to achieve commercialization are suggested.

2. Properties of halide perovskite materials

2.1 Crystal structures of halide perovskite materials

The ideal crystal structure of halide perovskite ABX_3 at high temperatures, an analogue to calcium titanate ($CaTiO_3$) perovskite, has a cubic symmetry and can be regarded as a lattice-like framework composed of corner-sharing [BX_6] octahedrons in three-dimensional space, as shown in Fig. 1(a).[50] The 'A' site is an organic or inorganic cation (including $CH_3NH_3^+$, NH_2–CH=NH_2^+ or Cs^+), which is filled in the voids formed by the octahedral three-dimensional network. The 'B' site is a metal ion (such as Pb^{2+}or Sn^{2+}) that occupies the heart of the octahedron. The 'X' site is a halogen group, which is located at

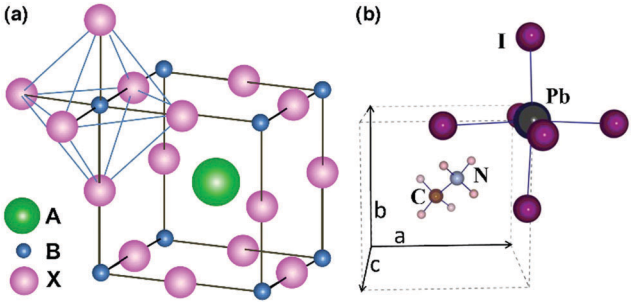

Fig. 1 (a) Crystal structure of ABX_3 perovskite, (b) a unit cell of cubic $CH_3NH_3PbI_3$ perovskite. Reproduced permission from ref. 50 Copyright 2015, Elsevier.

Table 2 Temperature-dependent crystal structural data of $MAPbX_3$ (X = Cl, Br, I)[52]

	$CH_3NH_3PbCl_3$ (K)	$CH_3NH_3PbBr_3$ (K)	$CH_3NH_3PbI_3$ (K)
Cubic	>178.8	>236.9	>327.4
Tetragonal	172.9–178.9	144.5–236.9	162.2–327.4
Orthorhombic	<172.9	<144.5	<162.2

the apexes of the octahedron. Fig. 1(b) shows a unit cell of cubic $CH_3NH_3PbI_3$. The A-site is a $CH_3NH_3^+$ cation and the B-site is a Pb^{2+} cation.[50] Such a structure is more stable than the face-shared or edge-shared crystal structures. Analogues of inorganic perovskites, a class of external stimuli (*i.e.*, temperature, light or pressure) can induce the phase transition from cubic to tetragonal or orthorhombic.[2,51–53] Temperature-dependent structural data of $MAPbX_3$ (X = Cl, Br, I) are listed in Table 2.[52]

Apart from external stimuli, the ionic radius, or more concisely the ratio of the cationic and anionic radii, is another important factor in the phase transition. The stability of a perovskite structure is mainly determined by the tolerance factor (t) and octahedral factor (μ). The t and μ are defined by eqn (1) and (2):[54–56]

$$t = \frac{R_A + R_B}{\sqrt{2}(R_B + R_X)} \quad (1)$$

$$\mu = \frac{R_B}{R_X} \quad (2)$$

where R_A, R_B, R_X denote the ionic radius of cations A, cations B, and anion X, respectively. Studies have shown that t for a stable structure of the halide perovskite is generally between 0.88 and 1.1, while μ is generally between 0.45 and 0.89.[56,57] When t is close to 1.0, the compound has an equi-axed crystal *Pm3m* structure in general. However, when t decreases below 1.0, which is the case with either a small A-ion or large B-ion, the cubic structure may change to tetragonal or orthorhombic structures.[58]

2.2 Physical properties of hybrid perovskite materials

Hybrid halide perovskites possess excellent physical properties, such as a low crystallization energy barrier, small exciton binding energy, long carrier diffusion length, large absorption coefficient, and excellent tolerance for defects, making them ideal active materials for solar cell applications. Table 3 summarizes relevant physical properties.

Table 3 Physical properties of hybrid perovskite materials

Physical properties	Value ranges
Crystallization energy barrier	56.6–97.3 kJ mol^{-1}
Trap-state density	$\sim 10^{10}$ cm^{-3} (single crystals), 10^{15}–10^{17} cm^{-3} (polycrystalline)
Carrier diffusion length	>1 μm (polycrystalline film)
Absorption coefficient	7×10^4 cm^{-1} at 600 nm ($CH_3NH_3PbI_3$)
Exciton binding energy	9–80 meV

(i) Low crystallization energy barrier. *In situ* X-ray scattering studies revealed that perovskite nucleation and crystallization activation energy is around 56.6–97.3 kJ mol^{-1}, which is much lower than that of amorphous silicon (280–470 kJ mol^{-1}).[17,18] Therefore, a perovskite film can be prepared by a series of low-temperature fabrication methods (such as a solution process), which shows great potential for industrial production.[59]

(ii) Low trap-state density. According to space-charge-limited current (SCLC) measurements and the aid of density functional theory (DFT), the trap density of polycrystalline perovskite films is in a range of 10^{15}–10^{17} cm^{-3}.[2] Perovskite single crystals grown at room temperature have an extremely low trap density of $\sim 10^{10}$ cm^{-3}, which is comparable to that of intrinsic crystalline silicon and much lower than a class of established and emerging semiconductors (including polycrystalline Si (10^{13}–10^{14} cm^{-3}), CdTe/CdS (10^{11}–10^{13} cm^{-3}), and CIGS (10^{13} cm^{-3})).[2,60–62]

(iii) Long carrier diffusion length. A long diffusion length of electron and hole helps to reduce charge recombination and enhance charge collection.[2,63] The minimum values of electron and hole diffusion lengths of $MAPbI_3$ are around 100–130 nm.[64] For a $MAPbI_3$ with large grain size, which was fabricated with a Cl^--based solution precursor, both electron and hole diffusion length can reach more than 1 μm, while the corresponding absorption depth is only around 100–200 nm.[65,66] To determine the limit of carrier diffusion length, Huang's group synthesized $MAPbI_3$, a single crystal *via* a solution-growth method, where both electron and hole diffusion length reached more than 175 μm.[61]

(iv) Large absorption coefficient. The absorption coefficient of $MAPbI_3$ was 1.5×10^4 cm^{-1} at 550 nm, roughly consistent with the value of 5.7×10^4 cm^{-1} at 600 nm. These values are an order of magnitude larger than that of silicon.[67–69] With a large absorption coefficient, efficient light harvesting can be obtained with a thin absorber and the thinner the absorber is, the smaller the charge recombination is ref. 2. Thus, a large absorption coefficient can not only help to capture light efficiently, but also improve the open circuit voltage (V_{oc}) of the solar cells.[70]

(v) Low exciton binding energy. Exciton binding energy is the energy required to dissociate excitons into free charge carriers, and a low exciton binding energy benefits reducing energy loss.[2] For example, the V_{oc} loss in OPVs is mainly due to a very large exciton binding energy ranging from 0.6 eV to 1.0 eV.[71]

According to different measurement methods, the exciton binding energy of perovskite materials is in the range of 9–80 meV.[72–76] Such a small exciton binding energy will contribute to small V_{oc} loss in PSCs.

3. The fabrication of perovskite films

Perovskite thin films are the most important part of PSCs and their quality acts as a decisive role in a device's performance. Up to now, various methods have been developed to fabricate perovskite thin films, and they can be categorized into two types: one-step deposition methods and two-step deposition methods.[77–81] In order to achieve high PCEs and further their commercialization, comprehensive analysis and reasonable control of the formation mechanisms are necessary.

3.1 One-step deposition

The formation process of perovskite crystals involved in a one-step deposition method involves a classical nucleation/growth crystallization mechanism which includes three stages: the solution reaches supersaturation, nucleation, and subsequent growth towards a large crystal.[82–85] The LaMer model in Fig. 2(a) schematically illustrates the nucleation and subsequent growth processes of the crystals.[85–87] A supersaturated solution is a prerequisite for nucleation. When the precursor solution is dropped on the substrate the solvent rapidly evaporates, the concentration of solute increases, and the solution quickly reaches saturation (C_s). Because there is a critical energy barrier, the nucleation process cannot happen at the saturation concentration (C_s). Only when the solvent continues to evaporate does a supersaturated solution (C_{min}^{nu}) exist with a Gibbs free energy higher than the surface energy of the newly formed nuclei. At this point the second stage, the nucleation process, begins and the atoms, ions, or molecules in the solution form a new phase as embryos or nuclei. The nucleation rate increases with increased supersaturation, so a higher supersaturation leads to a higher nucleation rate and density (more nuclei) and, thus, a larger number of smaller crystals. Once the nuclei are formed, then subsequent crystal growth proceeds immediately. With continuous consumption of the solute for formation of nuclei, the nucleation process terminates when the solution concentration is lower than C_{min}^{nu}. The crystal will continue to grow until the concentration of growth species drops below C_s. As shown in Fig. 2(b), once the nuclei are formed, subsequent growth occurs rapidly and simultaneously. Above the minimum concentration, nucleation and growth are indiscrete processes; however, their speeds are different. Subsequent growth contains two sequential and parallel steps: (i) the growth species diffuse to the growth surface and (ii) the surface growth, *i.e.*, the growth species are irreversibly incorporated to the kink, ledge-kink, and ledge sites of the crystal's growth surface. For a given solution concentration, high nucleation density leads to more nuclei. The final grain size depends on the nucleation density and subsequent solute supplement.

In classical nucleation theory, the nucleation rate (N) is affected by the nucleation factor (P) and the probability of atomic diffusion (Γ), so it follows from eqn (3):[83,85]

$$N = P\Gamma = \left\{\frac{C_0 KT}{3\pi\lambda^3\eta}\right\}\exp\left(\frac{-\Delta G^*}{kT}\right) \quad (3)$$

where λ is the nucleus diameter, η is the solution viscosity and C_0 is the initial solution concentration, and ΔG^* is the critical energy barrier. Eqn (3) shows that a high initial concentration or supersaturation helps to form more nuclei, while low viscosity or a critical energy barrier facilitates the diffusion of atoms/ions to the liquid–solid interface and then incorporation to the solid surface. In order to improve the coverage of high quality perovskite films, many efforts have been made to control the nucleation parameters (*e.g.*, volatility and solution viscosity (η)).[88–92]

For the fabrication of $MAPbI_3$ perovskite films, DMF, GBL, NMP, DMSO, and DMAc are the most commonly used solvents.[93–97] However, all these solvents have a rather high boiling point and low vapor pressure at room temperature. Slow evaporation of

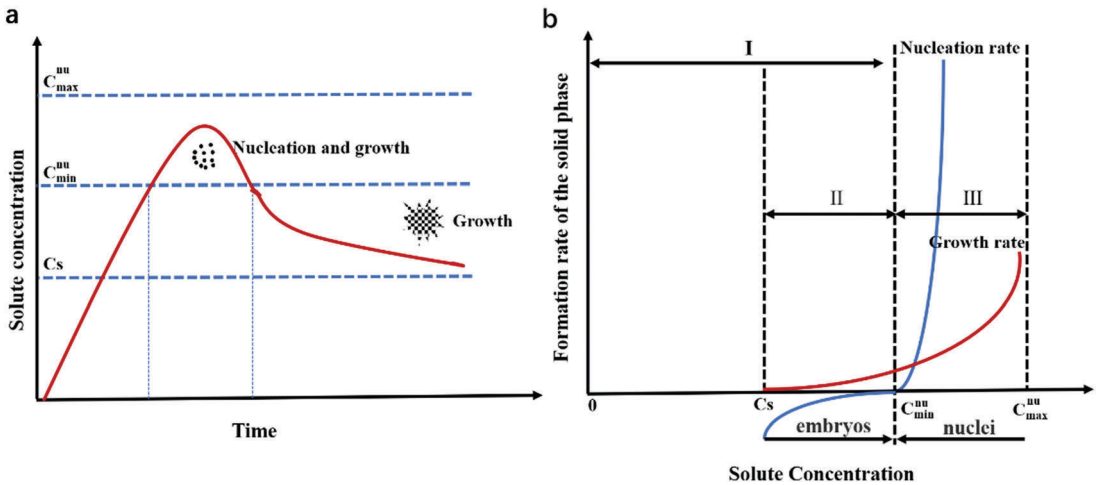

Fig. 2 (a) Schematic illustrating nucleation and subsequent growth processes. (b) Schematic illustrating relations of the nucleation and growth rates with solute concentration.

the solvent limits the nucleation rate which consequently leads to low nucleation density and fast crystal growth rate. When the DMF precursor solution ($MAI : PbI_2 = 1 : 1$, molar ratio) is spin-coated onto the substrate at room temperature, then a unique dendritic structure of $MAPbI_3$ film will be immediately formed due to low nucleation density and fast growth rate.[98] As shown in Fig. 3(e),[98] the branch-like crystal images display a low surface coverage. To solve this problem, in 2014 Xiao *et al.*[98] reported a one-step, anti-solvent-induced, fast crystallization deposition (FDC) method. This method involved spin-coating of the precursor solution followed by immediate exposure to chlorobenzene. The anti-solvent extracted the solvent quickly, resulting in a high degree of supersaturation of the solute, thus more crystal nuclei were generated. Dense and uniform perovskite films can be readily prepared by this method, as shown in Fig. 3(b). Although this process facilitates crystallization and generates a better film morphology, the quality of perovskite films and cell performance still vary appreciably with the additional time and amount of anti-solvent which makes this method difficult to control and hard to scale up.

In addition to the antisolvent method, hot-casting, gas-pumping, vacuum-pumping and gas flow methods were also used to tune the nucleation and grain growth process of perovskites.[89,99–104] Nie *et al.*[89] applied a hot-casting method to quicken evaporation of the high-boiling point solvents (NMP, B.P. 202 °C, or DMF, B.P. 150 °C), where pin-hole free and uniform perovskite films with crystalline grain sizes in the millimeter-scale were obtained. Fig. 3(c) shows a schematic illustration of the hot-casting method. The grain-size can be controlled by tuning the substrate temperature. As shown in Fig. 3(d), the grain size increased markedly with an increased substrate temperature. With the grain size increased from ~1 μm

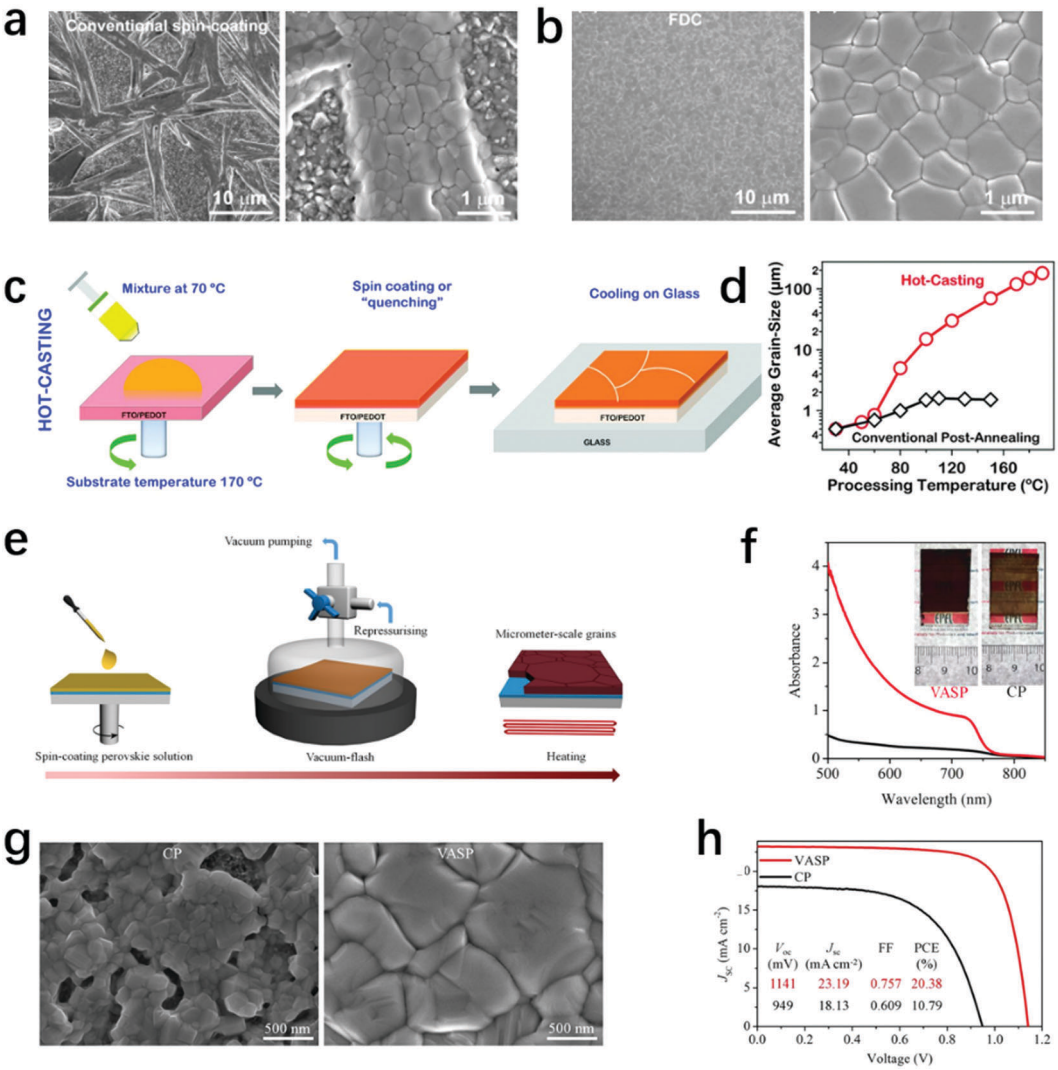

Fig. 3 SEM images of perovskite films prepared by one-step deposition methods. (a) Conventional spin-coating. (b) FDC (anti-solvent method). Reproduced with permission from ref. 98. Copyright 2014, Wiley. (c) Schematic illustration of the hot-casting process. (d) Variation of grain size as a function of substrate temperature. Reproduced with the permission from ref. 89. Copyright 2015, AAAS. (e) Schematic illustration of the deposition of a perovskite film *via* VASP. (f) UV-Vis and the photograph. (g) SEM images of the perovskite films. (h) *J*–*V* curves of PSCs prepared by CP and VASP methods. Reproduced with permission from ref. 99. Copyright 2016, AAAS.

to ~180 μm, the overall PCE increased from 1% to 18% due to reduced bulk defects. The authors attributed formation of large grains to a prolonged growth of the perovskite crystals. An excess solution present on the substrate kept supplying sufficient growth species for continuous crystal growth in an appropriate temperature window. A vacuum flash-assisted solution process (VASP) was also developed to enable rapid removal of solvent to generate a burst of supersaturation for rapid crystallization of the $FA_{0.81}MA_{0.15}PbI_{2.51}Br_{0.45}$ perovskite.[99] As shown in Fig. 3(e), the substrate was first spin-coated with perovskite solution and then placed in a vacuum chamber to allow rapid evaporation of the solvent. At last, the films were annealed at 100 °C for 30 min. As confirmed by the UV-Vis spectra and SEM images in Fig. 3(f) and (g), with the presence of Lewis acid–base DMSO as adduct, this method allows the deposition of large grain sized perovskite films with uniform coverage on the substrate compared with the conventional process (CP). A maximum PCE of 20.5% and a certified PCE of 19.6% was achieved for solar cells with a large square aperture area >1 cm^2. Furthermore, Ding *et al.*[86] developed a gas-flow-induced gas pump approach to regulate nucleation and grain growth of perovskite crystals and obtained dense, uniform, and full coverage large area perovskite films.

All the methods mentioned above would result in the rapid evaporation of solvent. The resulting supersaturation promotes rapid nucleation. The faster the nucleation rate is, the more crystal nuclei are generated, and the smaller the resultant crystals are. Although large grain sized perovskite films were obtained by effective control of the supersaturated solution, the mechanism of the formation of perovskite crystals from the precursor solution seems more complex as demonstrated by Pascoe's work.[82] They reported a nitrogen gas flow assisted method with post-annealing for fabrication of a perovskite film. Through precise control of the gas flow rate, the grain size of the produced perovskite films reached up to about 100 μm. However, their large grains were constituted of many smaller grains instead of being single mono-crystals. There are many factors affecting the film deposition process, *e.g.*, nitrogen gas flow may have generated prolonged supersaturation on the solution surface resulting in secondary or continued nucleation, and quick agglomeration of primary crystals may stop further growth with the depletion of growth species.

3.2 Colloidal chemistry and coordination interaction theory

In 2015, Yan *et al.*[105] revealed that perovskite precursor solutions are colloidal dispersions rather than real solutions, typically with colloidal particle sizes of 10–1100 nm. The organic component can coordinate with the inorganic component in a perovskite precursor to form colloidal particles, which serve as heterogeneous nucleation sites. The colloidal characteristics of the perovskite precursor solution was confirmed and further studied later by other groups.[36,106–110] Fig. 4(a) shows the Tyndall effect of different perovskite precursor solutions which indicates its colloidal characteristic.[108] Coordination between different components was confirmed by infrared spectroscopy (IR), as shown in Fig. 4(d). Due to different coordinations in different perovskite precursor solutions, the colloidal size will be different, as verified by the dynamic light scattering spectra in Fig. 4(b). With the addition of the CH_3NH_3Cl (MACl) additive to a standard perovskite precursor, the colloidal size significantly increased. When DMSO was further employed in the precursor, then the colloidal clusters characteristic was more stable. Based on such a colloidal engineering strategy and the coordination effects, large colloidal clusters with an average size close to the thickness of perovskite film will arrange on the substrate by spin-coating. After a following annealing process, with sublimation of the MACl, the intermediate phase transformed into perovskite crystals. Perovskite monolayer films with an average size of 3 μm were obtained as shown in Fig. 4(c).[108] Such perovskite films with large grain sizes show low trap-state density and high crystallinity. The PCE of the solar cell reached 19.14%. Such a coordination effect can combine with fast solvent evaporation methods (such as hot casting and vacuum evaporation) to obtain high quality perovskite films. For example, the combination of MACl coordination and heating assistance process (HAP) was demonstrated to result in a compact monolithic $MAPbI_3$ film.[107] Fig. 4(e) shows the schematic diagram of perovskite films prepared by MACl-HAP. As for MACl-HAP, MACl can coordinate with PbI_2·DMF·MAI to form coordination complexes in the precursor solution. Assisted by high temperature, the solvent evaporated quickly and the coordination intermediate frameworks grew up from the bottom to the top on the hot substrate. As shown in the top view and cross-sectional view SEM images (Fig. 4(f)), the average grain size of the monolithic film is about 3.6 μm. Almost no grain boundaries and pin-holes can be found in the cross profile. According to the space charge limited current (SCLC) in Fig. 4(g), the carrier mobility in the monolayer-like film was close to that in the $MAPbI_3$ perovskite single crystal and the trap density in the monolithic film was less than that of the control sample.

Based on the coordination interaction of different components and the colloidal characteristics of the precursor solution discussed above, the crystal size and crystallinity of perovskites can be controlled by adding additives. Micrometer scale perovskite films with high crystallinity were obtained with thiourea as an additive.[111] Thiourea can coordinate with MAI and PbI_2 to form the intermediate phase MAI·PbI_2·S = $C(NH_2)_2$, which would significantly impact the perovskite's crystallinity and morphology. An EA post-processing was applied to extract residual thiourea on the perovskite's surface or which was inserted in the grain boundary. Fig. 5(a) illustrates the reaction process of the monolithic perovskite grains. With the addition of thiourea, the crystal grain size increased substantially from 500 nm to over 2 μm, as shown in Fig. 5(b) and (c). After EA post-processing, the perovskite surface showed rough and striped microstructures (Fig. 5(d)). Based on such a monolithically grained perovskite film, the device showed excellent voltage response even under ultraweak light (0.05% sun).

The grain boundaries in a perovskite film are generally believed to responsible for charge carriers scattering and traps recombination.[12,112,113] Therefore, monolayer-like or monolithic perovskite films with a large grain size always show high

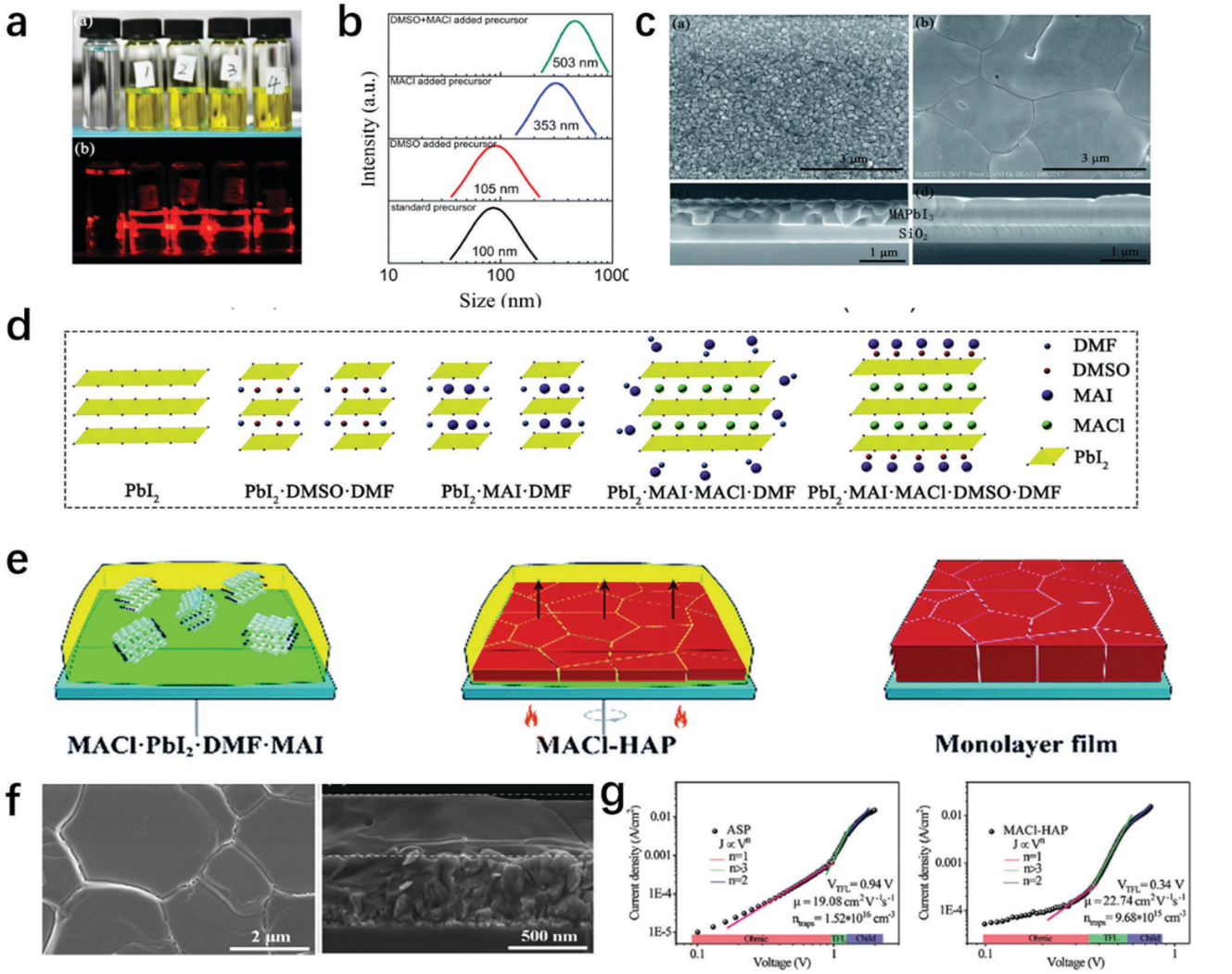

Fig. 4 (a) The Tyndall effect and (b) colloidal size distribution verified by dynamic light scattering spectra of different perovskite precursors. (c) SEM images of perovskite films prepared from precursors with addition of DMSO and DMSO + MACl. (d) Scheme of the coordination interaction in different colloidal precursors. Reproduced with permission from ref. 108. Copyright 2017, The Royal Society of Chemistry. (e) Schematic diagram of the formation of monolayer-like $MAPbI_3$ films by MACl-HAP. (f) Top-view and cross-sectional SEM images of perovskite films prepared by MACl-HAP. (g) Current density–voltage characteristics of devices with FTO/TiO_2/perovskite/PCBM/Au (electron-only devices). Reproduced with permission from ref. 107 copyright 2017, The Royal Society of Chemistry.

charge carrier mobility and low trap density and thus are considered as an ideal active layer for solar cells. From the above discussion, to optimize perovskite crystal growth, besides dropping anti-solvent during spin-coating, employing hot-substrate casting, and gas-pumping, vacuum-pumping, or gas flow methods, adding additives to a precursor solution has been proven as another effective method which was applied to control film morphology, such as surface uniformity, surface coverage, and crystal size for high performance.

3.3 Formation mechanisms in two-step deposition methods

For two-step deposition methods, lead halide is deposited on the substrate first, then organic halides either in solution or in vapor, intercalate into the layered lead halide crystals to form perovskite films.[78,114–117] The conversion process is a heterogeneous reaction between the solid lead halides layer and organic halide solution or vapor. Two formation mechanisms of the $MAPbI_3$ perovskite have been proposed: one is a direct solid–liquid interfacial reaction at low MAI concentration and the other is a dissolution–crystallization at high MAI concentration.[78,118] Fu *et al.* further studied these two formation mechanisms in two-step deposition method.[119] As shown in Fig. 6(a), when the MAI concentration is no more than 8 mg mL^{-1}, then an *in situ* transformation (interfacial reaction) proceeds in within 2 min according to eqn (4). When the MAI concentration is higher than 10 mg mL^{-1}, then $MAPbI_3$ perovskite crystals form immediately *via* a solid–liquid interfacial reaction. A further reaction of MAI with underlying PbI_2 is suppressed leading to an incomplete reaction. When the MAI concentration is high ($\geq$20 mg mL^{-1}), then formed crystalline $MAPbI_3$ crystals and the underlying PbI_2 will react with I^- to form PbI_4^{2-} according to reactions (5) and (6). When the PbI_4^{2-}

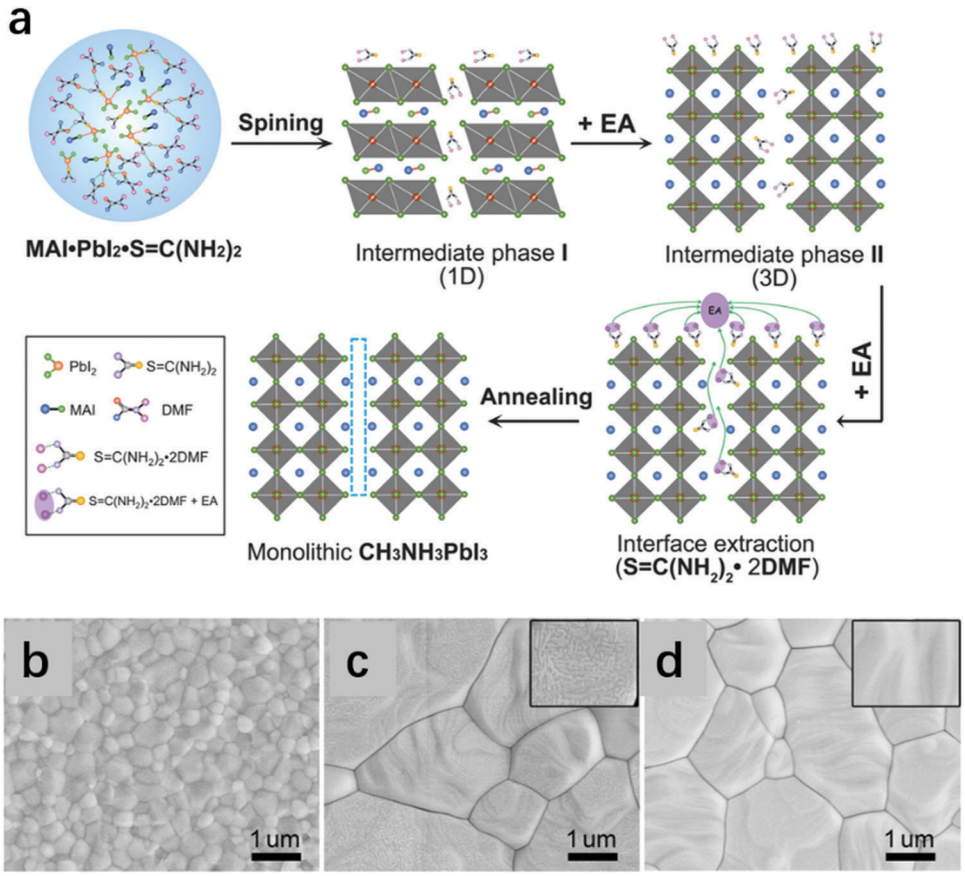

Fig. 5 (a) Schematic illustration of the reaction process from the precursor to monolithic perovskite grains. SEM images of perovskite films prepared from (b) pristine perovskite precursor, (c) thiourea-containing perovskite precursor, (d) thiourea-containing perovskite precursor (EA post-processing). Reproduced with permission from ref. 111. Copyright 2017, Wiley.

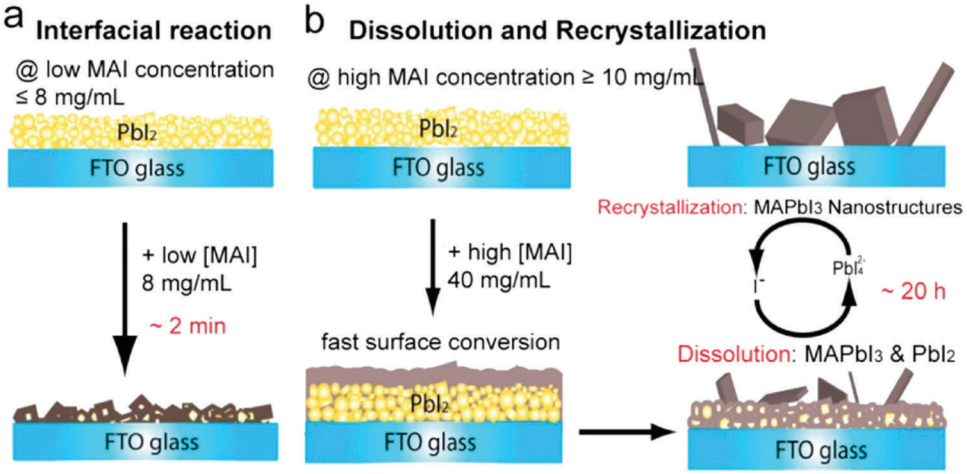

Fig. 6 Schematic illustration of the two growth mechanisms involved in two-step deposition methods for crystalline $MAPbI_3$ perovskites. (a) Solid–liquid interfacial reaction mechanism at a lower MAI concentration, and (b) dissolution–recrystallization growth mechanism at a higher MAI concentration. Reproduced with permission from ref. 119. Copyright 2017, American Chemical Society.

concentration reaches saturation, then PbI_4^{2-} will react with MA^+ to recrystallize and form large $MAPbI_3$ crystals as shown in Fig. 6(b). Since the interfacial reaction conversion is much faster than dissolution–recrystallization growth, it often requires more than one hour to fully convert PbI_2 into a $MAPbI_3$ crystal film. Thus, the main problems for a two-step deposition method are the long conversion time and the incomplete conversion of PbI_2. The long conversion time leads to uneven distribution of large

crystals because of the Ostwald ripening. The incomplete conversion of PbI_2 leads to the presence of unreacted PbI_2 in the perovskite. And it was also suggested by Rahimnejad *et al.*,[120] that incomplete conversion of PbI_2 also leads to undercoordinated lead species which would act as structural defects and increase charge recombination. All these problems would severely deteriorate a resulting device's performance.

$$PbI_2(s) + MA^+(sol) + I^-(sol) \rightarrow MAPbI_3(s) \quad (4)$$

$$MAPbI_3(s) + I^-(sol) \rightarrow MA^+(sol) + PbI_4^{2-}(sol) \quad (5)$$

$$PbI_2(s) + 2I^-(sol) \rightarrow PbI_4^{2-}(sol) \quad (6)$$

To overcome the long conversion time and incomplete conversion issues, fabricating a porous PbI_2 layer with post-treatment, constructing an intermediate phase, and additive control methods were applied to increase the contact area between PbI_2 crystal and MAI solution.[121–124] Besides fabricating a porous PbI_2 layer, retarding the crystallization of PbI_2 or pre-expanding the PbI_2 layered structure are effective methods to get good crystallinity and a smooth surface.[125,126] Wu *et al.*[125] used DMSO instead of DMF as solvent to dissolve PbI_2. Due to the strong coordination effect of DMSO with Pb^{2+} ions, the crystallization of PbI_2 was successfully retarded as illustrated in Fig. 7(a). Compared with the layered crystals of the DMF-based PbI_2 film, the amorphous DMSO-based PbI_2 films show a more uniform surface (Fig. 7(b)). The amorphous DMSO-based PbI_2 can completely convert into a uniform $MAPbI_3$ perovskite film within a short time (10 min). As a result, the solar cells obtained from DMSO based PbI_2 show better performance compared with that obtained from DMF-based PbI_2 (Fig. 7(c)). Another more successful work was reported on fabrication of the $FAPbI_3$ perovskite through an intramolecular exchange process (IEP) between DMSO and FAI.[126] In this work, a PbI_2(DMSO) precursor solution was prepared. As illustrated in Fig. 7(e) and (f), the DMSO molecules are embedded between the edge-sharing $[PbI_6]$ octahedral layers and expand the PbI_2 layered structure. After exposing the PbI_2(DMSO) precursor solution to FAI, a $FAPbI_3$ perovskite film was formed *via* IEP within 1 min. The final perovskite films show a dense and uniform surface with larger grains compared with that prepared *via* a conventional method (Fig. 7(g)). A significantly improved PCE of 20.1% was obtained by this method (Fig. 7(h)).

Other strategies including controlling the precursor's composition or improving conversion techniques have been used to improve the conversion rate of PbI_2 and the quality of a perovskite film.[79,127–129] For example, a dynamic growth method (DGM) was introduced to prepare $MAPbI_3$ perovskite films.[129] Fig. 7(d) shows the static growth method (SGM) and DGM fabrication process. Compared with SGM, the DGM helps to the eliminate the concentration gradient at the PbI_2/CH_3NH_3I interface and produces more nuclei during the nucleation and growth of perovskite crystals to eliminate pinholes. Compact perovskite films were obtained by DGM. Many efforts have been

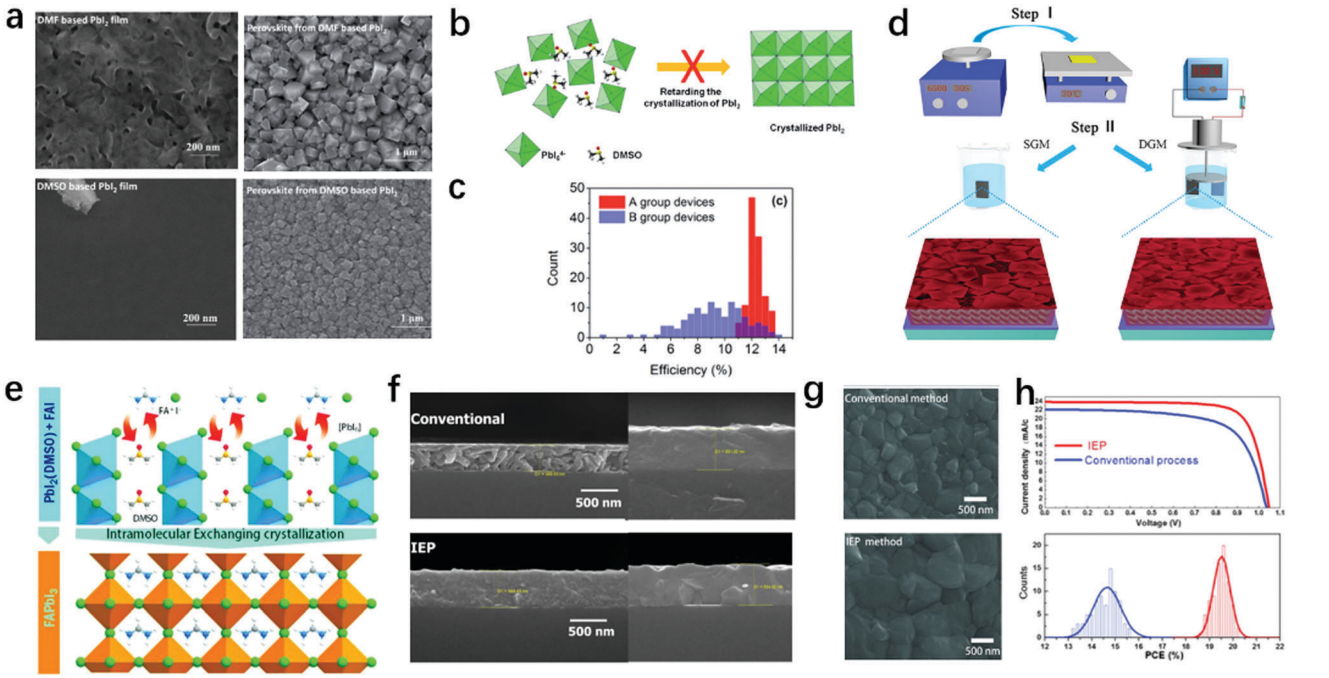

Fig. 7 (a) SEM images of the DMF-based PbI_2 film and DMSO-based PbI_2 film. (b) Schematic illustration of the strongly coordinated DMSO solvent used to retard the crystallization of PbI_2. (c) PCE distribution of the solar cells fabricated from DMF-based PbI_2 film and DMSO-based PbI_2 film. Reproduced with permission from (a–d) ref. 125, Copyright 2014, RSC. (d) The SGM and DGM fabrication processes of perovskite films. Reproduced with permission from ref. 129, Copyright 2016, American Chemical Society. (e) Schematic illustration of the intramolecular exchange crystallization of $FAPbI_3$. (f) The cross-sectional SEM images before and after the conversion process, (g) a comparison of the SEM images of the $FAPbI_3$ perovskite, (h) J–V curves of the $FAPbI_3$-based PSCs fabricated with IEP and a conventional process. Reproduced with permission from (e–h) ref. 126, Copyright 2015, AAAS.

made to improve the quality of two-step deposited perovskite films and device efficiencies of more than 20% were obtained. This method seems to not be commonly used due to its more complicated reproducibility compared with one-step deposition.

4. Up-scaling of perovskite film fabrication

The unique properties and easy manufacturing of organic–inorganic hybrid perovskite materials and their excellent device performance offer a great promise for successful commercialization of PSCs. At present, the spin-coating method is widely used in the preparation of PSCs. However, it is difficult to prepare a high quality perovskite film with a large area and utilization of the precursor solution is very low. Thus, it is inappropriate for large-scale commercial production. In spite of intensive efforts that have been made to explore a suitable large-scale fabrication method (including roll-to-roll process, spray-coating, doctor-blade coating, *etc.*) for perovskite films, the PCEs of the produced solar cells are still lower than those of spin-coated devices. Therefore, it is urgent to take measures to improve the PCEs of PSCs made by the deposition processes that tolerate up-scaling, especially when we consider that the performance of solar cells is mainly predetermined by the quality of the perovskite crystal films. Several promising up-scalable fabrication techniques are discussed below.

4.1 Soft-cover deposition

The soft-cover deposition (SCD) method works by covering a soft film with high surface wettability, such as polyimide (PI) and polytetrafluoroethylene (PTEE), on the top of perovskite drops under heat treatment. This method allows rapid solvent evaporation and nucleation when the soft-cover is peeled off. The resulting perovskite films show good uniformity and high quality. This process can be conducted in normal environment with a high materials utilization rate up to 80%, which may be suitable for large-scale fabrication.[130–132] Ye *et al.* prepared $MAPbI_3$ perovskite films with this method and obtained a 17.6% PCE with a working area of 1 cm^2.[130] The fabrication process is shown in Fig. 8(a). First, the substrate is heated to a specific temperature (150–270 °C) for 30–60 s. Then the precursor solution is added to the center of the substrate. After that, a polyimide (PI) soft film is used to cover to the liquid precursor. After about 25 s, a computer-controlled mechanical hand was employed to peel off the soft film from one side at a specified speed. Fig. 8(b) shows one droplet of the perovskite precursor. The left half is under the soft-cover and the right half is the crystallized perovskite crystal after peeling off the soft-cover.

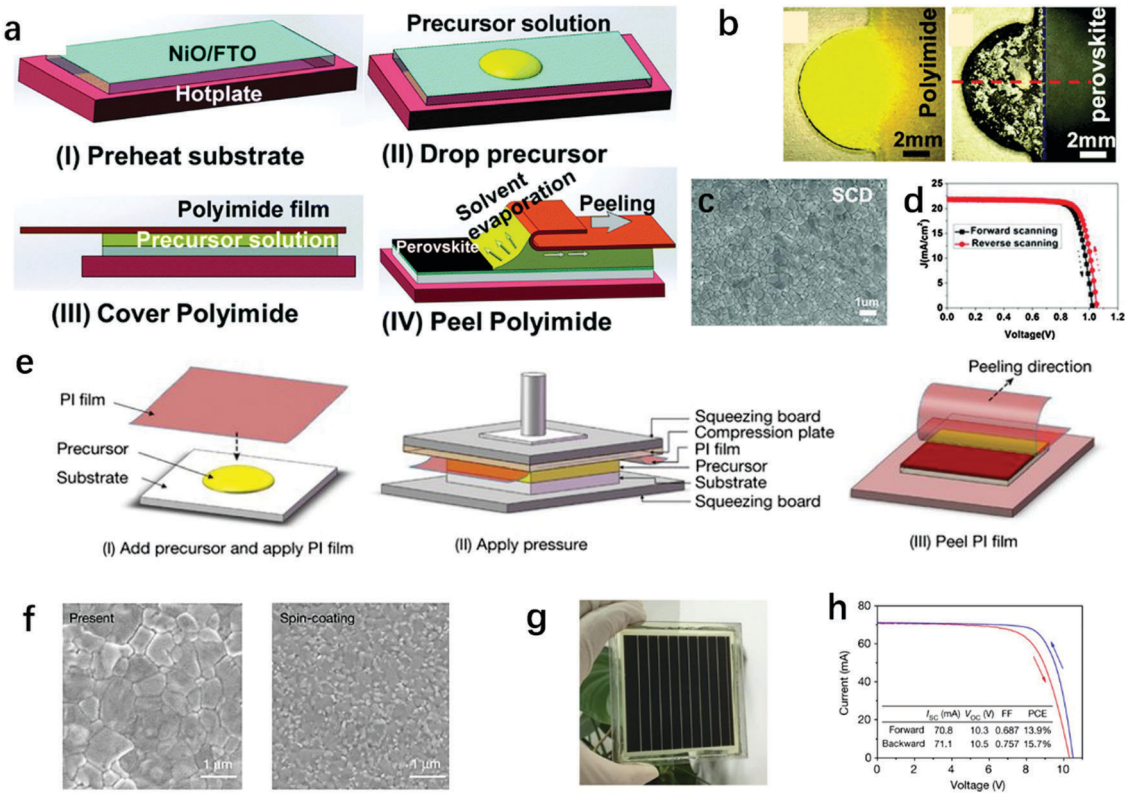

Fig. 8 (a) Schematic illustration of the SCD method. (b) One droplet of perovskite precursor with half under the soft-cover (left) and the crystallized perovskite film after peeling off the soft-cover (right). (c) SEM image of perovskite films prepared by the SCD method. (d) *J*–*V* curves of the PSC prepared by the SCD method. Reproduced with permission from ref. 130. Copyright 2016, The Royal Society of Chemistry. (e) Schematic diagram of the preparation process. (f) The top-view SEM images of the perovskite film. (g) Photograph of the perovskite module. (h) *J*–*V* curves of the solar module. Reproduced with permission from ref. 132. Copyright 2017, Springer Nature.

The heterogeneous nucleation seems to occur at the interface between substrate and precursor solution. With the solvent evaporating quickly after peeling off the soft cover, the crystallization is likely to take a directional growth. The applied soft cover also helps to improve the precursor solution's wettability on the substrate. A surface coverage close to 100% with large grain sizes ranging from 500 nm to 1.2 μm was obtained as shown in Fig. 8(c).

Following this work, Ye *et al.*[131] further developed a low temperature (80 °C) soft-cover deposition method and obtained a high PCE of 15.5% for the solar cell with a large working area of 5 cm^2. This low temperature process was successfully applied on flexible substrates and obtained a PCE of 15.3% with a 0.09 cm^2 working area. Recently, dense and uniform perovskite films were obtained with an improved soft-cover deposition method, which was performed in an air conditioned room at ambient temperature.[132] This method was assisted with pressure treatment to convert the amine complex precursor into a perovskite film. The amine complex precursors of $PbI_2{\cdot}CH_3NH_2$ (1 : 1, molar ratio) and $CH_3NH_3I{\cdot}3CH_3NH_2$ (1 : 3, molar ratio) were obtained by directly reacting PbI_2 powder with CH_3NH_3I powder or CH_3NH_2 gas. As shown in Fig. 8(e), the mixed amine complex precursors were loaded on the center of the substrate and then a polyimide (PI) film covered the precursors. The liquid precursor spread under the PI film assisted by pressure from the pneumatically driven squeezing board. Before peeling off the PI film, the pressure was kept for 60 s and the film was heated at 50 °C for 2 min. When peeling off the PI film, the CH_3NH_2 gas was released due to the weak molecular interaction, and a dense and homogeneous perovskite film was formed as shown in Fig. 8(f). The reaction process can be described by the following formulas (7)–(9):

$$CH_3NH_3I + mCH_3NH_2 = CH_3NH_3I{\cdot}mCH_3NH_2 \quad (7)$$

$$PbI_2 + nCH_3NH_2 = PbI_2{\cdot}nCH_3NH_2 \quad (8)$$

$$CH_3NH_3I{\cdot}mCH_3NH_2 + PbI_2{\cdot}nCH_3NH_2 \rightarrow CH_3NH_3PbI_3 + (m+n)\,CH_3NH_2\uparrow \quad (9)$$

As shown in Fig. 8(g) and (h), a certified PCE of 12.1% with an aperture area of 36.1 cm^2 was achieved. It was the highest certified efficiency for perovskite solar modules at that time.

This soft cover deposition method is capable of low-cost fabrication of high performance perovskite solar cells. However, there are still challenges to obtain high quality perovskite films with high material utilization ratios. Surface wettability, solution viscosity, and selection of a soft cover are the key factors to modulate. More research studies are still essential to further enlarge the device's working area without reducing the PCE.

4.2 Drop casting on screen-printed scaffolds

Perovskite infiltration on screen-printed scaffolds *via* a drop casting method was first developed by Han and co-works in 2014. The perovskite layer was directly infiltrated into a mesoporous TiO_2 and ZrO_2 double layered scaffold as shown in Fig. 9(a), which avoided the requirement of a hole-conducting layer.[133] The solution infiltrated into the porous TiO_2/ZrO_2 scaffold due to the capillary force of the micropore structures. Then, 5-ammoniumvaleric acid (5-AVA) iodide was applied as an additive to the $MAPbI_3$ perovskite precursor solution and served as nucleation sites and template to promote the formation of $(5\text{-AVA})_x(MA)_{1-x}PbI_3$ perovskite crystals with preferable growth direction. Compared with the $MAPbI_3$, the $(5\text{-AVA})_x(MA)_{1-x}PbI_3$ perovskite showed better pore filling and a much lower defect concentration as well as better contact with the TiO_2 scaffold (Fig. 9(b)). A certified PCE of 12.8% was achieved for the solar cells and they remained stable for more than 1000 hours in ambient air under full sunlight illumination.

Based on the same method, Han *et al.*[134] proposed a production line for large-scale perovskite solar modules as shown in Fig. 9(c). A screen-printed TiO_2/ZrO_2/carbon triple layer framework was applied as a scaffolder and $(5\text{-AVA})_x(MA)_{1-x}PbI_3$ perovskite was drop-casted onto the carbon side of the film. In this method, carbon works as counter electrode to avoid using a hole

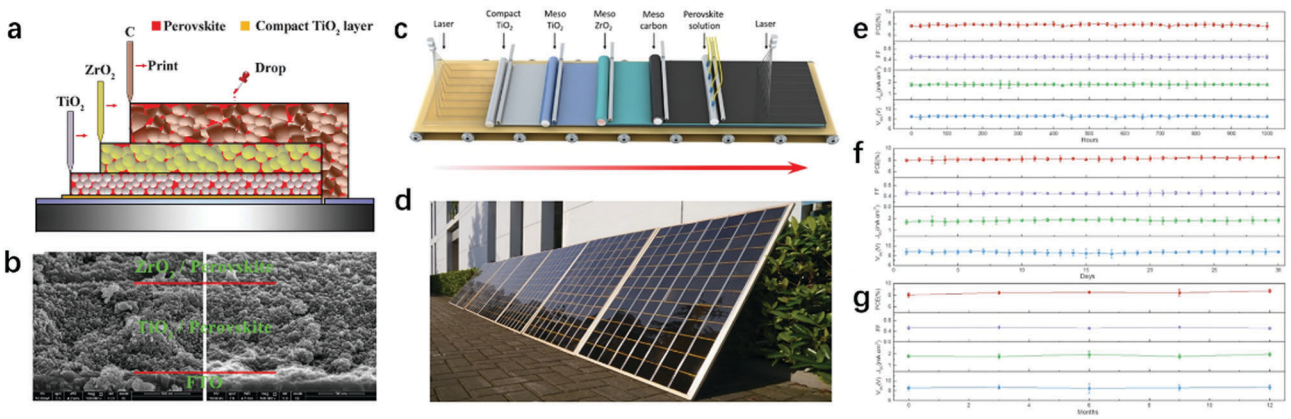

Fig. 9 (a) Schematic illustration of perovskite infiltration on screen-printed scaffolds *via* the drop casting method. (b) SEM images of the cross section of $MAPbI_3$- and $(5\text{-AVA})_x(MA)_{1-x}PbI_3$-based perovskite mesoscopic solar cells. Reproduced with permission from ref. 133. Copyright 2014, AAAS. (c) Schematic illustration of the solar module production line. (d) Image of a monolithic printed perovskite solar module with 10 sub-cells. The evolution of the average photovoltaic parameters of three PSCs along with their standard deviation under different conditions. (e) at 100 mW cm^{-2}, (f) during outdoor aging in Wuhan, China and (g) in the dark for 1 year. Reproduced with permission from ref. 134. Copyright 2017, Wiley.

conductor or Au reflector. The perovskite solar modules (10 × 10 cm^2) consisted of 10 serially connected cells with an active area of 49 cm^2 (Fig. 9(d)) and showed a 10.4% PCE. Under AM1.5 illumination, although the surface temperature of the solar modules reached 50 °C, they can stabilize for 1000 h under conditions with a temperature of 25 °C and humidity of 54% as shown in Fig. 9(e). Fig. 9(f) shows the performance of the encapsulated devices working on the lab roof from April 22nd to May 23rd, 2016 in the local environment of Wuhan, China. There's almost no degradation. The unsealed modules were kept stable in the dark for over 1 year as shown in Fig. 9(g). A fully printed 7 m^2 perovskite solar panel was also fabricated, which showed good reproducibility for manufacturing. In the meantime, Subodh's group[5] fabricated a 70 cm^2 perovskite solar module with the same structure. It worked in ambient conditions for more than 2000 h and the efficiency had less than a 5% reduction.

Drop casting a perovskite precursor on a screen-printed scaffold is an effective method for preparing perovskite solar modules and has the advantages of being low cost, easy regulation, and enabling large-scale fabrication. However, the PCEs of these solar cells are still much lower than those fabricated with a conventional spin coating method. The mesoscopic layer and the properties of the precursor solution critically determine the perovskite filling fraction and its quality. To realize a controllable fabrication, it is better to construct an auto production line.

4.3 Inkjet printing

Compared to traditional printing technology, inkjet printing is a digital method, which can be controlled by a computer program to obtain the desired patterns. Inkjet printing has no special requirements for the shape and materials (such as paper, silk, or metal) of the substrate due to its non-contact process. Moreover, inkjet printing can realize printing in different places and support remote network transmission printing due to its digital management technology.[135] The most common inkjet-printing methods today are continuous inkjet printing and drop-on-demand printing, as shown in Fig. 10(a).[136] For liquid piezoelectric inkjet printing, the working process can be divided into three stages: (1) the piezoelectric element is slightly shrunk under the control of a signal and then results in a larger extension, (2) pushing out the ink droplets from the nozzle, and (3) the components shrink again when the ink droplets fly away from the nozzle. In this way, the ink droplets have a required shape and a correct flight direction. In 2014, Wei *et al.* fabricated $TiO_2/CH_3NH_3PbI_3$/C structured PSCs by an inkjet printing method as shown in Fig. 10(b) and obtained a PCE of 11.6%.[137] However, in this work, a PbI_2 layer was still prepared by a spin-coating method. An improved inkjet printing process was developed to prepare a $MAPbI_3$ perovskite as shown in Fig. 10(c).[21] The influences of substrate wettability, ink droplet wetting behavior, and viscosity and solvent evaporation rate on the quality of perovskite films were investigated. It was found that the mesoporous TiO_2 substrate was better than the smooth compact TiO_2 with better wettability. When the volume ratio of the solvent DMF and DMSO was 1 : 1, then the ink droplet could get an optimal viscosity and evaporation rate. With the precise control of the micro-droplet size by inkjet-printing, uniform sized PbI_2 grains were obtained as shown in Fig. 10(d). Followed by MAI vapor treatment, compact perovskite films with crystalline grain sizes in micro-scale were obtained, which enabled a high PCE of 17.74% for a large area (2.02 cm^2) (Fig. 10(e)).

The inkjet printing method mentioned above was only applied for a MAI or PbI_2 deposition. In 2016, a single-step inkjet-printed PSC with 11.3% PCE was demonstrated. As shown in Fig. 10(f), a vacuum drying and annealing process was applied to promote the nucleation and crystallization. This work represents a meaningful progress towards commercialization.[138] However, the PCE was still lower than that prepared with spin coating. Controlling perovskite crystallization during an inkjet printing process still remains a challenge. A more successful attempt was made by Liang *et al.* in 2018.[21] Solvent composition optimization and vacuum-assisted thermal annealing post-treatment methods were combined in the inkjet printing process. The PSCs based on printed $CH_3NH_3PbI_3$ showed a high PCE of 17.04% for 0.04 cm^2 and 13.27% for 4.0 cm^2 with negligible hysteresis (lower than 1.0%).

Although the inkjet printing method shows potential with large scale fabrication of perovskite thin films, many challenges still remain to be solved. It's still very difficult to get high performance PSCs with uniform and compact crystallized perovskite films. Both the perovskite inks and printing parameters affect ink-drop formation, droplet wetting behavior on substrates, and subsequent film formation is still needed to optimize fabricate defect-free uniform perovskite thin films.

4.4 Doctor-blade coating

Doctor-blade deposition is a simple and versatile continuous fabrication method. This method is widely applied in the fabrication of thin films, especially the TiO_2 mesoporous layer in dye-sensitized solar cells and quantum dot-sensitized solar cells.[139,140] Compared with the spin-coating method, this technique works by swiping the precursor solution on the substrate with a blade and allows a scalable fabrication. In 2015, a doctor-blade coating method was applied with PSC fabrication for the first time. However, the film showed poor quality.[19] Then, through tuning the perovskite composition and adding a MACl additive, smooth and compact $MA_{0.6}FA_{0.38}Cs_{0.02}PbI_{2.975}Br_{0.025}$ films were obtained *via* the blade-coating method.[141] Fig. 11(a) illustrates the blade-coating and perovskite crystallization processes. The blade swipes a perovskite precursor solution (ink) on a hot substrate (~100–140 °C). The hot substrate speeds up solvent evaporation and the diffusion of growth species, promotes nucleation, and subsequent growth. MACl was applied as an additive to form intermediate phases. As shown in Fig. 11(b), without MACl additive, the perovskite film consists of many small grains with size distribution in the range of 100–400 nm and shows low surface coverage. When MACl additive was added into the precursor, the grain size significantly increased to micrometers, as shown in Fig. 11(c) and a stabilized PCE of 19.3% was obtained. Without the adding of MACl, perovskite films with large grain size, uniform coverage, and high crystal quality

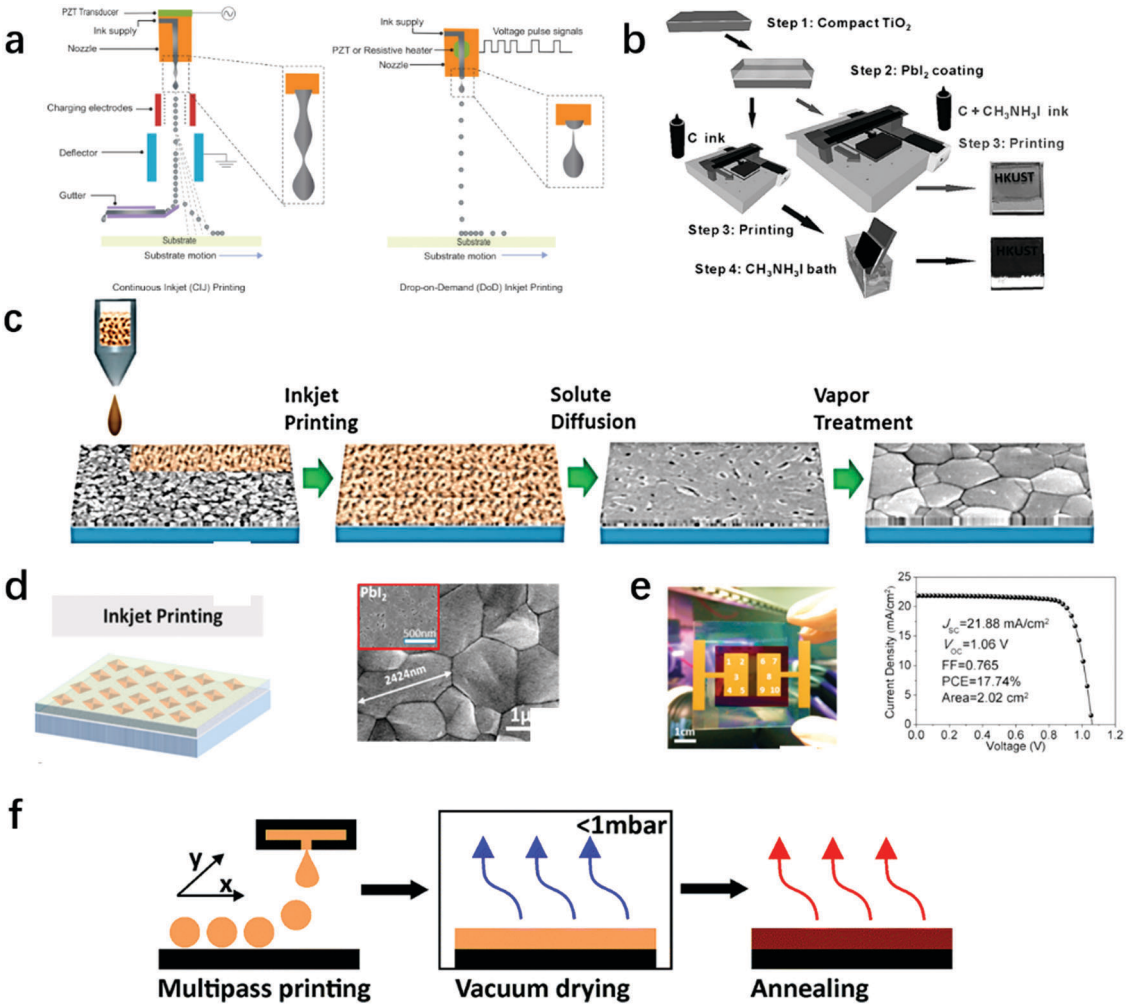

Fig. 10 (a) Schematic diagram of inkjet printing methods. Reproduced with permission from ref. 136, Copyright 2017, Wiley. (b) Fabrication process of the PSCs with ink jet printing. Reproduced with permission from ref. 137, Copyright 2014, Wiley. (c) Schematic illustration of perovskite films fabrication process. (d) Diagram of the PbI_2 distribution on m-TiO_2 and surface morphology of PbI_2 film. (e) The diagram of large-area PSCs with an active area of 2.02 cm^2 and its J–V curves. Reproduced with permission from ref. 21. Copyright 2018, Elsevier. (f) Schematics of the inkjet printing process with vacuum drying and thermal annealing. Reproduced with permission from ref. 138, Copyright 2016, The Royal Society of Chemistry.

were also obtained.[142,143] For example, through controlling the intermediate phase transition which arises from the difference in solvent extraction, Li *et al.*[142] blade-coated $MAPbI_3$ films and produced solar cells with a high efficiency of 18.74% (0.09 cm^2) and 17.06% (1 cm^2). They found that fast removal of the solvents would promote the phase transition from a sol–gel precursor to $MAPbI_3$ crystals directly without the formation of a solvated intermediate phase. Fig. 11(d) shows the real-time optical microscopy of the perovskite precursor solution with DMSO and GBL as solvent casted on the substrate. Spherulitic growth occurred around the centered nuclei. The Voronoi cell diagram in figure (e) illustrates the $MAPbI_3$ spherulitic film. The perovskite grains grew within Voronoi cells and growth was governed by solute diffusion. Fig. 11(f) shows the surface morphology of the perovskite film, which shows uniform coverage and large grain size.

Similarly, a meniscus-assisted solution printing (MASP) method was investigated to yield high crystallization perovskite films with a large grain size as shown in Fig. 12(a).[144] This method is similar to the doctor-blade coating. Fig. 12(b) shows that the perovskite precursor ink was constrained between a substrate and a plate and a meniscus was formed owing to capillary action. An outward convective flow would facilitate crystal growth, which was formed due to the fast solvent evaporation on the edge of the meniscus. With this method, micrometer-scale perovskite grains with good crystallinity were obtained (Fig. 12(c)) and the efficiency exceeded 20% for planar solar cells as shown in Fig. 12(d). In this work, optical microscopy was applied to track growth kinetics of the perovskite crystals. The perovskite grains were spherulitic growth and can be illustrated by a Voronoi cell diagram. The result suggested that nucleation density depends on the outward convective flow driven by evaporation within the meniscus ink, and a faster outward flow leads to higher nucleation density. And nucleation density significantly impacts the final perovskite crystal size where, with a lower nucleation density, larger crystals can be formed

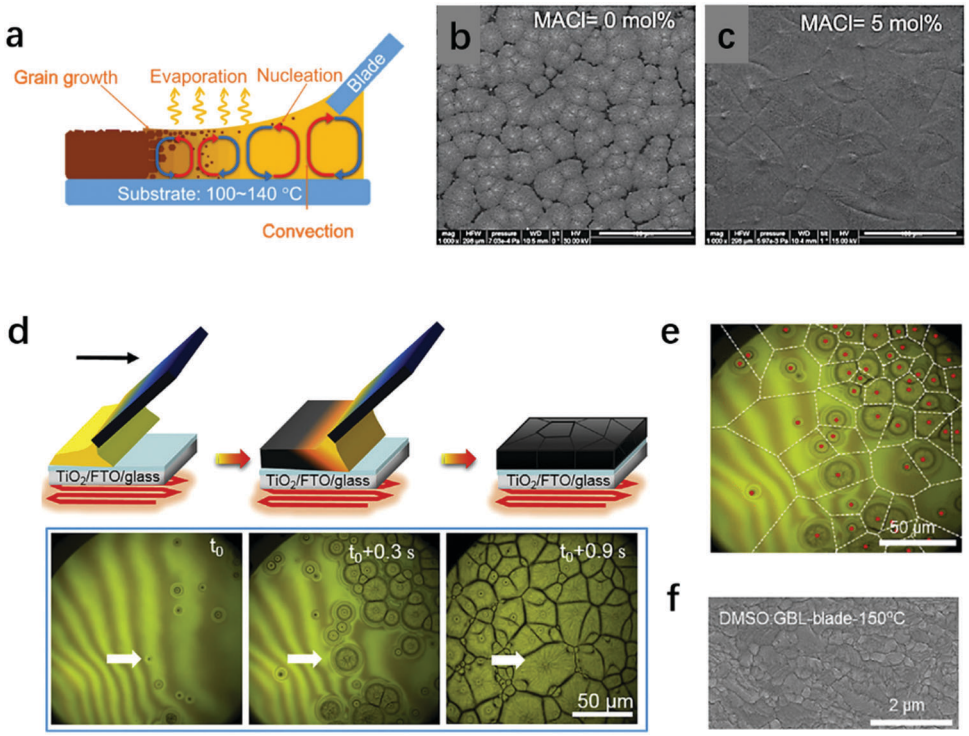

Fig. 11 (a) Schematic illustration of the crystallization of perovskite crystals during the doctor-blading process. SEM images of perovskite films (b) without MACl additive and (c) with MACl additive. Reproduced with permission from ref. 141. Copyright 2017, Wiley. (d) Schematic of the doctor-blading deposition (DMSO:GBL-blade-150 °C) process and real-time optical microscopy. (e) Voronoi cell diagram of $MAPbI_3$ spherulitic film for the representative DMSO:GBL-blade-150 °C case. (f) SEM image of the $MAPbI_3$ perovskite film. Reproduced with permission from ref. 142, copyright 2018, Elsevier.

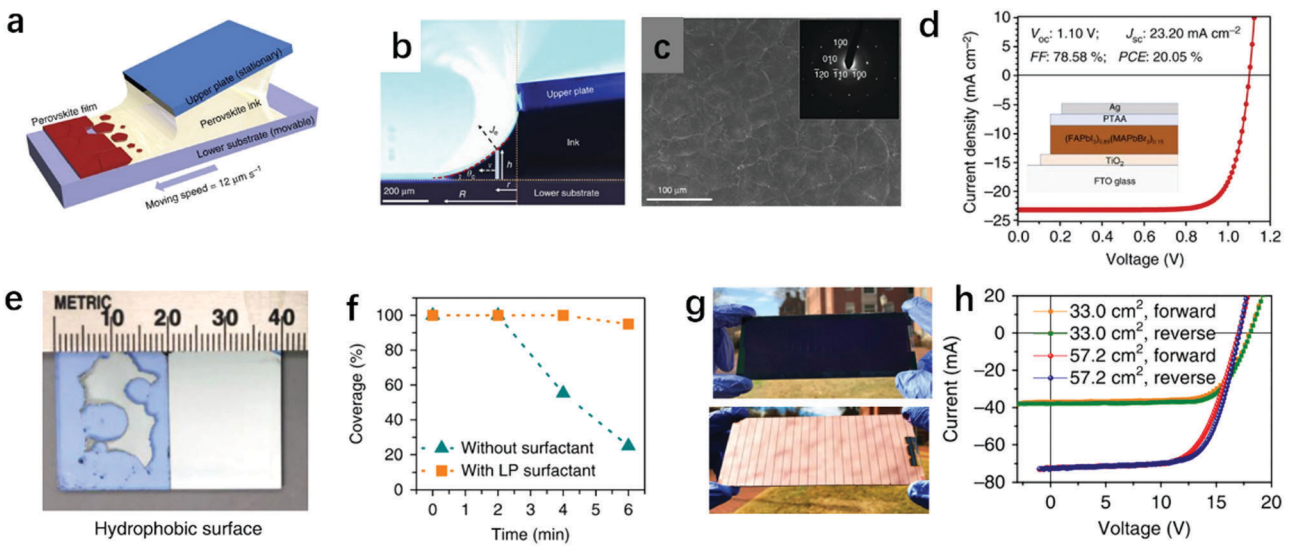

Fig. 12 (a) Schematic illustration of meniscus-assisted solution printing (MASP). (b) Optical micrograph of the side-view meniscus ink confined between a lower flat, movable, substrate, and the upper stationary plate. (c) SEM image of a perovskite film made by MASP. (d) *J*–*V* curves of the planar solar cell. Reproduced with permission from ref. 144, Copyright 2017, Springer Nature. (e) Pictures of blade-coated perovskite films on non-wetting substrates, and (f) perovskite droplets coverage evolution during the drying process without and with LP surfactant. (g) *J*–*V* curves at the maximum power point of modules with aperture areas of 33.0 cm^2 and 57.2 cm^2. (h) Photos of a perovskite solar module viewed from the glass side and top electrode side. Produced with permission from ref. 145, Copyright 2018, Springer Nature.

due to fewer competitors for solutes during crystal growth. The outward flow can be adjusted by solvent density, meniscus height, substrate temperature, and the substrate's moving speed.

Additional progress was made by Huang's group in the fabrication of large scale perovskite films *via* the doctor blading method.[145] A very small amount of surfactants (*e.g.*, L-α-phosphatidylcholine (LP))

was included as an additive into the perovskite precursor solution. Compared with the normal solution, the LP surfactant increased the wettability of the precursor solution on the underlying non-wetting charge transport layer as shown in Fig. 12(e). The coverage of the droplet remained almost 100% as shown in Fig. 12(f). The LP surfactant also altered the fluid drying dynamics during the whole drying period, which enabled blading of high quality perovskite films with low surface roughness at a high coating speed of 180 m h^{-1}. The surfactant can also passivate charge traps and efficiencies over 20% for small-area solar cells were obtained. Fig. 12(g) shows a perovskite solar module fabricated on a 6 × 15 cm^2 glass substrate and its sub-cells have a width of 0.65 cm and are connected in series. The module with aperture areas of 33.0 cm^2 and 57.2 cm^2 show stabilized efficiencies of 15.3% and 14.6% as shown in Fig. 12(h), respectively.

Compared with the spin-coating process, the doctor-blading method can realize temperature control during film formation. And it's easier to control evaporation and fluid dynamics of the precursor solution. According to the above discussion, the performance of devices fabricated *via* a doctor blade method can be improved by the following aspects: (1) controlling physical factors (such as substrate surface energy, solution surface tension, and viscosity) to improve film quality, (2) constructing the colloid precursor instead of a general precursor solution. The synergy of colloidal chemistry and coordination interaction theory can be effectively employed to improve the doctor-blade coating process.

4.5 Brush-painting

The "brush-painting (BP)" method, which is one of the most traditional forms of paintings in China, also has been investigated to fabricate perovskite solar cells and modules. The fabrication tool is a "Maobi" or "zhushua," also called a "Chinese ink brush."[146] Lee *et al.*[147] prepared all brush-painted PSCs, with the exception of an evaporated metal electrode, yielding a 9.08% PCE on an ITO substrate and a 7.75% PCE on a flexible substrate. A schematic illustration of the procedure of the brush-painting process and chemical structures of the main solvents and additive are shown in Fig. 13(a). The thickness and morphology of perovskite films can be controlled by the precursor solution concentration and substrate temperature. Lee's group investigated effects of the solvents *N*,*N*-dimethylformamide (DMF) and 2-methoxy ethanol (2-ME), which have different volatilities, on the morphology of perovskite films and the PSC's performance. Fig. 13(b–d) and (e–g) show the SEM images

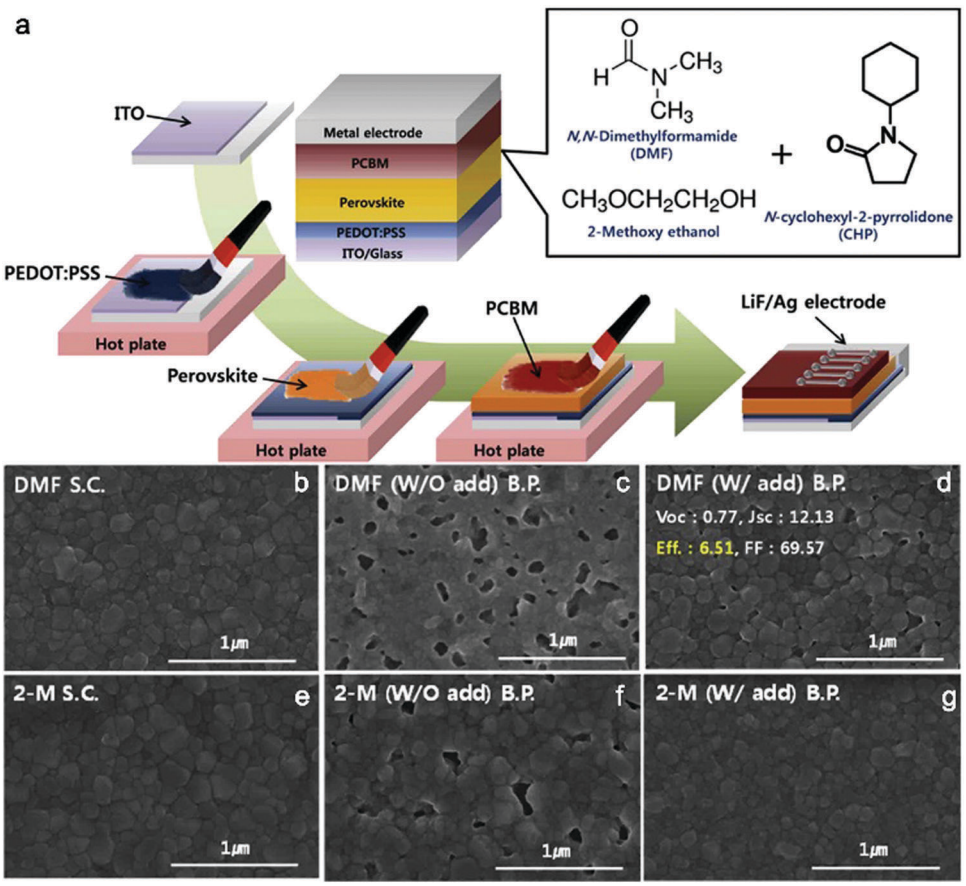

Fig. 13 (a) Schematic illustration of an all brush-painted planar heterojunction PSC process; SEM images of a perovskite film fabricated by (b), (e) spin-coating and (c, d, f and g) the brush-painting method with different solvents and additives. Reproduced with permission from ref. 147. Copyright 2017, Elsevier.

of the perovskite films prepared with the BP method using DMF or 2-ME solvent, respectively. The highly volatile nature of 2-ME promoted the nucleation. Thus, the surface coverage of the film with 2-ME solvent was found to be better than that prepared with DMF solvent.

Brush-painting is an inexpensive method with advantages of high material utilization ratio, ease of patterning, and suitable for large-area production. However, the quality and thickness of a perovskite film is difficult to be controlled accurately from coating speed and substrate temperature. In addition, toxic effects of processing solvents and chemicals hinder the use of this method. In the future, if green substitutions for the toxic Pb^{2+} and solvent is found, then the brush-painting process will be closer to commercialization.

4.6 Spray-coating

Spray-coating deposition technology has been intensively studied in the fabrication of organic photovoltaic (OPV) and oxide thin films.[148–154] This method also attracted attention with the fabrication of perovskite thin films.[155,156] As shown in Fig. 14(a), the experimental apparatus of the spray-coating method is similar to that of the inkjet-printing method, being mainly composed of an atomizing system and a deposition system.[157] The two systems are connected by a quartz nozzle, which is fitted with the perovskite precursor solution. An ultrasonic atomizer disperses the perovskite precursor into small droplets, and then a low-pressure gas stream directs them to the substrate. As the solvent evaporates, the perovskite films are formed by depositing on the substrate. In recent years, great efforts have been made with spray coating perovskite solar cells, especially controlling the crystallization of perovskites.

As early as 2014, Barrows *et al.* prepared the planar structured $CH_3NH_3PbI_{3-x}Cl_x$ PSC by a spray-coating method for the first time and achieved an 11% PCE.[158] In this work, the effects of substrate temperature, spray solvent volatility, post deposition annealing time, and temperature on the morphology and surface coverage of the perovskite were explored. As shown in Fig. 14(b–d), the crystallite size and surface coverage were different with different substrate temperatures due to different nucleation and crystallization rates. After optimization, a film with highest coverage of 85% was observed at a substrate temperature of 75 °C.

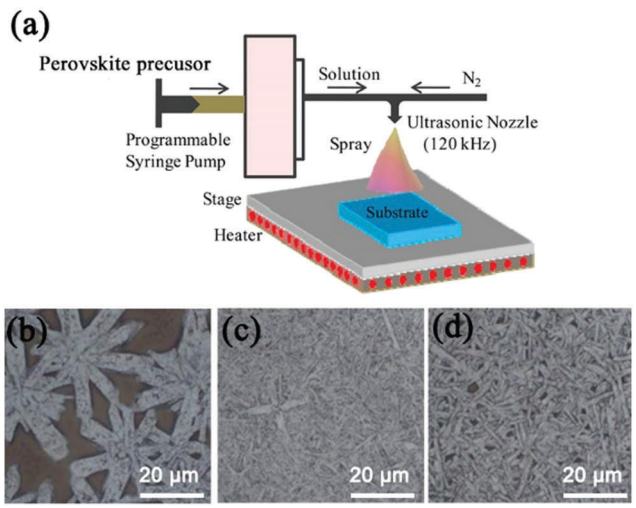

Fig. 14 (a) Schematic illustration of a spray-coating system. Reproduced with permission from ref. 157, Copyright 2015, American Chemical Society. (b–d) SEM images of perovskite films with substrate temperatures of 28 °C, 75 °C and 87 °C. Reproduced with permission from (b–d) ref. 158, Copyright 2014, The Royal Society of Chemistry.

In order to prepare uniform and pin-hole free perovskite films, it is necessary to investigate characteristics of the precursor liquid drops during a spray-coating process in detail. The surface tension of a liquid drop is an important factor in determining film quality. A large surface tension means poor wettability of the liquid, which tends to produce a spherical cap shape rather than a continuous wet layer on the substrate. Adding a surfactant or another solvent with a small surface tension to form a two-solvent system can reduce the liquid's surface tension. In 2016, Ishihara *et al.* studied the fluid dynamics of droplets in the spray-coating process.[159] The solvent volume ratio of NMP (with surface tension of 40.79 mN m^{-1} at 20 °C) and DMF (with surface tension of 37.1 mN m^{-1} at 20 °C) was varied to generate a local surface tension gradient. Therefore, droplets could spread into a continuous wet film on the substrate so as to achieve complete surface coverage of the perovskite films. The PCE of the PSC prepared with the two-solvent system reached 14.2%, 1.5 times of that made with the one-solvent spray pyrolysis. The velocity related to the spreading capabilities of the two-solvent system is defined by eqn (10):[160,161]

$$v_c^2(x) = \frac{1}{2\eta(x)}\frac{d_r}{d_x}x(1-x)(-A_l\alpha_l + A_h\alpha_h) \qquad (10)$$

where η is the viscosity of the film, γ is the surface tension, x is the volume fraction of the low surface tension solvent, and A_l, α_l, and A_h, α_h are the evaporation rates and the activity coefficients of solvents with low and high surface tension, respectively.

To construct a two-solvent system with small surface tension, the other solvent added in the solution must meet the following conditions:

(i) it is miscible with the original solvent,

(ii) it can dissolve the solutes, and

(iii) its boiling point is lower than that of the original solvent.

Heo *et al.*[162] spray coated pre-synthesized $MAPbI_{3-x}Cl_x$ perovskite powder on a substrate and obtained perovskite films with large grain size by balancing the inward flux (F_{in}) with the outward flux (F_{out}). In this work, a two-solvent system containing the low boiling point solvent DMF and high boiling point solvent GBL with a volume ratio of 8 : 2 was applied to obtain the largest perovskite crystal with an average grain size of 1.5 μm. Fig. 15(a–c) show the film morphologies of the perovskite films from different spray times. In the early stage, small perovskite grains were formed. Then, with the replenishment of the $MAPbI_{3-x}Cl_x$ powder solution, the small grains were re-dissolved and re-crystallized into larger grains. The crystallization process is illustrated in Fig. 15(d). When $F_{in} \ll F_{out}$, then the injected perovskite solution crystallizes directly on the perovskite film surface before penetrating the bottom of the film. However, when $F_{in} \gg F_{out}$,

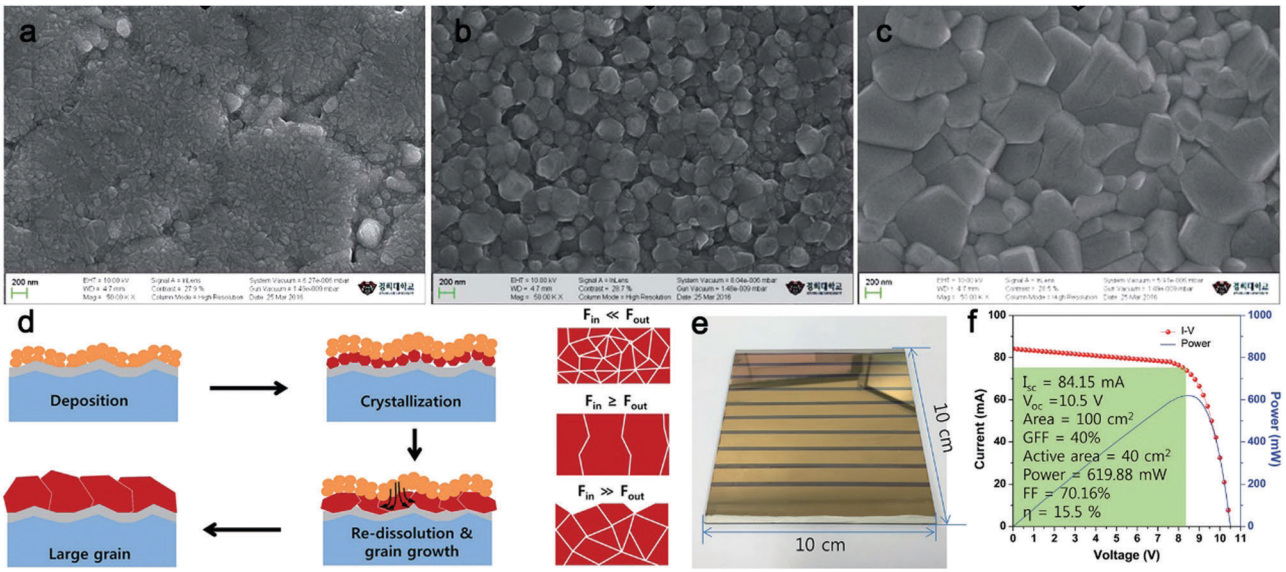

Fig. 15 SEM images of the produced perovskite films with different spray times: (a) 30 s, (b) 60 s, and (c) 90 s. (d) Schematic illustration of perovskite crystalline grain growth and the morphology change which depends on the balance between F_{in} and F_{out}. (e) Photograph of the sub-module PSCs based on a spray-coating method and (f) J–V curves. Reproduced with permission from ref. 162. Copyright 2016, The Royal Society of Chemistry.

then the bottom of the film cannot completely dry during the spraying process, thus forming fewer grains due to rewetting. When F_{in} is slightly higher or similar to F_{out}, then the continuously sprayed perovskite solution can wet the underlying perovskite layer, and the crystallites can re-dissolved and grow to a monolayer-like $MAPbI_{3-x}Cl_x$ film by recrystallization. Fig. 15(e) and (f) show photographs of the FTO/TiO_2/$MAPbI_{3-x}Cl_x$/PTAA/Au planar solar sub-module (10 cm × 10 cm) which consists of 10 sub-unit cells and its photovoltaic properties. A high PCE of 15.5% was obtained for the sub-module, and its PCE reached 18.3% for the sub-unit cells which was the highest efficiency attained for spray-coated perovskite solar cells.

Recently, Habibi *et al.*[163] further improved the spray-coating fabrication process through optimizing the substrate temperature and perovskite solution concentration. They carefully investigated influence of the perovskite solution concentration on the surface tension, viscosity, and contact angle and pinhole-free perovskite thin films ($CH_3NH_3PbI_{3-x}Cl_x$) with large-area (25 cm^2) were obtained.

There is great potential for the spray-coating method to achieve cost-effective, large-area, and efficient PSCs. A PCE from a perovskite solar module fabricated *via* the spay-coating method is relatively low. Optimizing spraying speed, substrate temperature, distance between the nozzle and substrate, and properties of the perovskite precursor solution can improve the film quality and thickness. Low utilization of the precursor solution is also a big barrier for this method towards commercialization. In the future, we expect more efforts to realize a high flux spray pyrolysis process that will prepare cost-effective perovskite solar modules with high PCEs.

4.7 Slot-die coating

The slot-die coating method has been successfully applied with large-scale fabrication of organic photovoltaic devices.[164,165] This method is similar to the blade coating method, except that the ink leaks out from the ink reservoir through a thin slit to the substrate. Vak *et al.* applied a 3D printer linked slot-die coater, which accurately controlled the x, y, z positions, nozzle temperature, and bed to fabricate perovskite solar cells, except the evaporating metal electrode.[20] The perovskite films were fabricated with a two-step deposition method but only the PbI_2 layer was prepared by the slot-die coating method. Fig. 16(a) illustrates the slot-die coating process. Combined with a gas-quenching process to promote nucleation, a pinhole-free PbI_2 layer was obtained. Photographs of PbI_2 films and their corresponding SEM images under various coating conditions are shown in Fig. 16(a–d), respectively. If the film was naturally dried without gas quenching then, due to a slow nucleation rate and fast crystallization, branch-like crystals will appear (Fig. 16(b)). With gas-quenching, the films showed a dense surface with good uniformity (Fig. 16(c)). However, to fully convert PbI_2 into a perovskite film, MAI must permeate the PbI_2 layer. However, the gas-quenched film was too dense to react with MAI completely so they put the film in a small enclosed sample carrier to stop the continuous solvent evaporation coating and then gas-quenching was completed. As shown in the photograph of Fig. 16(a), the film turned cloudy. According to the corresponding SEM images in Fig. 16(d), the cloudy film showed an ideal state because it was not only sufficiently dense to stop formation of pinholes but also had micro cracks large enough to facilitate the infiltration of MAI molecules. As a result, an 11.96% PCE was achieved.

In 2017, Weihua Solar Co., Ltd, in Xiamen, China cast a 40% $CH_3NH_3PbI_3$/DMF precursor solution on the substrate with this method.[166] As shown in Fig. 16(e), the slot-die coater was assisted with a gas pump system to allow rapid evaporation of the DMF solvent. They obtained large-area perovskite

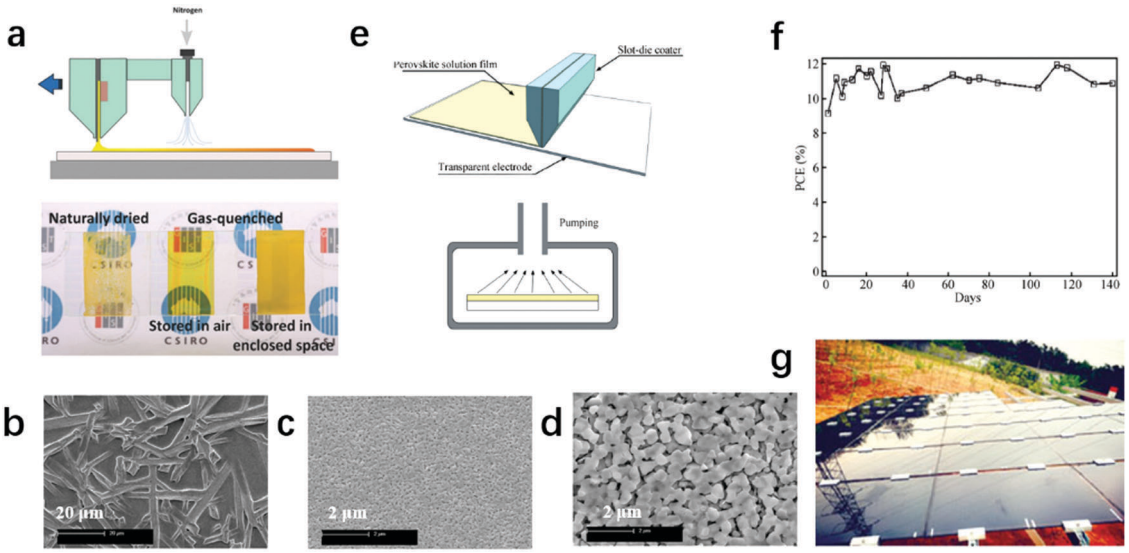

Fig. 16 (a) Schematic illustration of slot-die coating with a gas-quenching process and photographs of the produced PbI_2 films under different coating conditions: (b) naturally dried PbI_2; the gas-quenched glassy PbI_2 film stored (c) in air, and (d) in enclosed space. Reproduced with permission from ref. 20. Copyright 2015, Wiley. (e) Scheme of perovskite film preparation procedures. (f) PCE evolution of a 5 × 5 cm^2 module recorded within 140 days; (g) the demonstration power plant. Reproduced with permission from ref. 166. Copyright 2017, Elsevier.

modules ranging from 5 × 5 cm^2 to 45 × 65 cm^2 and demonstrated the power plant in Fig. 16(g). The PCE of the 5 × 5 cm^2 module reached 10.6% and showed good reproducibility. Almost no degradation was observed after 140 days of outdoor testing, as shown in Fig. 16(f). Recently, Giacomo[167] developed a sheet-to-sheet slot-die coating process to fabricate a perovskite photoactive layer and the hole transport layer. The large area modules (12.5 × 13.5 cm^2) on 6 inch × 6 inch substrates demonstrated PCEs above 10%, with a power output of 1.7 W.

Compared to other coating methods, slot-die coating has a much higher material consumption rate, because all the injected solution can be transferred to the substrate. Apart from a higher material usage rate, the film can be prepared in a fully enclosed space, which can avoid leakage of harmful perovskite precursors. Finally, the parameters of a perovskite thin film can be precisely controlled by the feeding pump pressure, slot width, viscosity of solution precursor, and coating speed. However, this requires strict demands for the ink quality. In addition, the perovskite film quality was still worse than that prepared by spin coating at a laboratory scale. Colloidal chemistry and coordination interaction theory can be used to further optimize the perovskite crystallization process.

4.8 Challenges for large-scale fabrication of perovskite thin films

The scalable fabrication processes of PSCs have attracted much more attention accompanied with rapidly increased PCEs. Many research institutes and scientific technical companies have made considerable efforts to advance them. Table 4 summarizes the device structures, device working areas, perovskite formation techniques, and device performances of perovskite solar cells with different active area fabrication methods. We also drew a plot to show the relationships between device area and PCEs of the devices prepared by various fabrication methods as shown in Fig. 17. The red points represent solar modules and PCEs fabricated by different scalable fabrication methods. We can see that the larger the active area is, the lower the PCE is. PCEs of solar modules with an active area of more than 10 cm^2 have difficulty in exceeding 16%. But solar modules with a relatively large area (> 30 cm^2) and a PCE around 15% can be achieved by doctor-blade coating, soft-cover deposition, and spray coating methods. Thus, doctor-blade coating, soft-cover deposition, and spray coating methods are more likely to achieve high performance PSC modules.

There are still a number of obstacles to overcome for the scalable fabrication of perovskite thin films: (1) the low efficiency of the devices with a large active area as well as poor film quality, (2) precursor solutions with uncontrollable reproducibility are usually a complication for commercialization due to fast nucleation and growth rates of perovskites crystals, and (3) low raw material utilization. Therefore, the focus of current perovskite studies should be dedicated to developing reliable equipment and to control precursor solution properties to enable high quality large-scale manufacturing using low-cost materials, environmentally-friendly production, efficient stock utilization, and enhanced PCE.

5. Obstacles and progress toward PSC commercialization

Despite the attractive combination of physical properties of organic–inorganic halide perovskites including intrinsic broad and strong optical absorption, high charge carrier mobility, low exciton binding energy, long free carrier diffusion length, and high PCEs from resulting PSCs, there are obstacles and hurdles toward the PSCs' full commercialization. For example,

Table 4 Summary and comparison of device structures, device working area, perovskite formation techniques, and device performances of large scale perovskite solar cells fabricated by various fabrication methods including M-module, CE-certified efficiency, PV-perovskite, and 2D-two dimensional

Methods	Device structures	Scale (cm^2)	PCE (%)	Ref. (publish year)
Doctor-blade coating	TiO_2/PV/spiro	1.0	11.70	100 (2017)
Doctor-blade coating	TiO_2/PV/spiro	0.1	13.3	103 (2015)
		10.1-M	10.4	103 (2015)
		100-M	4.3	103 (2015)
Doctor-blade coating	PTAA/PV/fullerene (C60)/ bathocuproine (BCP)	33-M	15.3	145 (2018)
		57.2-M	14.6	145 (2018)
Doctor-blade coating	SnO_2/PV/spiro	10-M	12.31	168 (2018)
Brush-painting	PEDOT/PV/PCBM	0.0464	9.08	147 (2017)
Drop casting on screen-printed mesoscopic holder	TiO_2/ZrO_2–PV/C	4.9	14.02	169 (2017)
		49-M	10.4	169 (2017)
Drop casting on screen-printed mesoscopic holder	TiO_2/ZrO_2–PV/C	30-M	10.46	5 (2016)
		70-M	10.74	5 (2016)
Soft-cover deposition	TiO_2/PV/spiro	1	19.3	170 (2017)
		36.1-M	15.7 (12.1-CE)	170 (2017)
Soft-cover deposition	NiO/PV/PCBM-BCP	1.0	17.6	130 (2016)
Soft-cover deposition	NiO/PV/PCBM-BCP	5.0	15.5	131 (2017)
Soft-cover deposition	NiO/PV/PCBM-BCP	5	15.5	131 (2017)
Spray-coating	PEDOT/PV/PCBM	0.025	11	158 (2014)
Spray-coating	TiO_2/PV/PTAA	40-M	15.5	162 (2016)
Spray-coating	PEDOT/PV/PCBM	0.025	11.4	171 (2016)
Spray-coating	PEDOT/PV/PCBM-C-BCP	1	12.2	172 (2016)
Spin-coating-VASP (vacuum lash-assisted solution process)	TiO_2/PV/spiro	1	19.6-CE	99 (2016)
Spin-coating-GP (gas pump)	ZnO/PV/spiro	0.1	19	173 (2016)
		1.13	13.91	173 (2016)
Spin-coating-GP (gas pump)	TiO_2/PV/spiro	0.1	20.44	86 (2017)
		1	17.03	86 (2017)
Spin-coating	NMLO/PV/PCBM	1.02	16.2 (15-CE)	174 (2015)
Slot-die coating	PEDOT/PV/PCBM	0.1	15.57	91 (2018)
Slot-die coating	ZnO/PV/carbon	25	10.6	166 (2017)
Slot-die coating	TiO_2/PV/spiro	168.75-M	11	167 (2018)
Inkjet-printing	TiO_2/PV/spiro	0.04	17.04	175 (2018)
		4	13.27	175 (2018)
Spin-coating	TiO_2/PV/PTAA	1	19.7-CE	80 (2017)
Spin-coating	PFN/PV/PCBM	1	17.04	176 (2017)
Spin-coating	TiO_2/PV/spiro	1	18.32	177 (2017)
Spin-coating	SnO_2/PV/spiro	1	20.1-CE	178 (2017)
Spin-coating	TiO_2/PV/spiro	4-M	13.6	179 (2016)
Spin-coating	TiO_2/PV/spiro	1.01	16.61	180 (2017)
Spin-coating	TiO_2/PV/spiro	1.10	19.5-CE	181 (2017)
Spin-coating	NiO/PV/PCBM-BCP	1.022	18.21-CE	182 (2016)
Spin-coating	TiO_2/PV/spiro	1.05	15.89	183 (2017)
Spin-coating	PCBM/PV/PTAA	1.20	15.98	184 (2016)
		5.04	12.79	184 (2016)
Spin-coating	PEDOT/PV(2D)/PCBM	2.32	8.77	185 (2016)
Spin-coating	PEDOT/PV/PCBM	60-M	8.7	186 (2014)
Spin-coating	PEDOT/PV/PCBM	40-M	11.9	187 (2015)

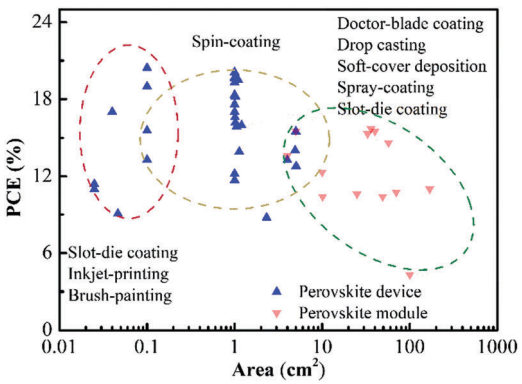

Fig. 17 The plots summarize and compare device areas and PCEs with various fabrication methods.

organic–inorganic halide perovskites lack stability when subjected to exposure to oxygen, moisture, high temperature, and UV irradiation. In comparison with Si solar cells with more than 20 years of operation lifetime, the deficiency of long-term stability of hybrid perovskite materials is the greatest barrier towards commercialization of PSCs. The toxicity of lead and its detrimental effects on the environment can't be ignored and the toxicity of solvents, additives, and precursors used during the fabrication process should be addressed as well. Another important aspect which should be considered is the module cost.

5.1 Stability issues

The deficiency of long-term stability of a hybrid perovskite material has become one of the greatest barriers to the commercialization

of PSCs. In contrast, hybrid perovskite materials are ionic crystals and the organic and inorganic components are bonded by hydrogen bonds or van der Waals forces. They readily and sensitively respond to even subtle changes in ambient environment; for example, humidity, temperature, oxygen content, and UV light.[188] Phase transition occurs easily and they are easy to decompose into their inorganic components due to the loss of organic components from an external stimulus.[34,188–190] Many methods have been developed to improve the long-term stability of hybrid perovskite materials. Tuning the perovskite component, constructing a two-dimensional perovskite, post treatment, encapsulation, and device architecture modifications are considered as the most effective strategies to protect perovskite structures from inside and outside forces.[191–194]

The most important strategy for achieving stable solar cells is to improve intrinsic stability of the materials. Considering the volatility and thermal instability of the MA cation, replacing it with a larger and heavier (formamidinium, $NHCHNH_2$) FA cation is an effective way to increase stability.[195–197] The relatively narrow band gap of $FAPbI_3$ permits broader absorption of the solar spectrum which helps to obtain high device performance. However, $FAPbI_3$ forms a non-perovskite yellow film consisting of a hexagonal phase at room temperature due to the FA cation's large size. Annealing above 150 °C (tetragonal phase transition temperature) forms a black perovskite phase which is retained after cooling to room temperature where the hexagonal phase is still present and its fraction increases over time, leading to a serious decrease in device performance. Combination of the larger FA cation with the smaller Cs cation on the A site to form $FA_{1-y}Cs_yPbI_3$ can tune the tolerance factor close to 1 as shown in Fig. 18(a), allowing formation of the desired black perovskite phase. Fig. 18(b–f) clearly show that the $FA_{1-y}Cs_yPbI_3$ perovskite exhibits enhanced phase stability and enhanced thermal stability.[54] Macmeekin's group[198] showed that $FA_{0.83}Cs_{0.17}Pb(I_{1-x}Br_x)_3$ perovskite did not degrade even after annealing at 130 °C for 6 hours under inert conditions. To replace the volatile organic A cation with inorganic Cs to make all inorganic perovskites is another way that has been attempted to enhance thermal stability.[199–201]

Two-dimensional Ruddlesden–Popper perovskites have attracted increasing research attention in recent years.[202] The general formula of a 2D perovskite is $(RNH_3)A_{n-1}B_nX_{3n+1}$ (n = 1, 2, 3, 4...), where R is an aromatic group or long-chain alkyl and n presents the thickness of the perovskite sheets between the organic chains.[203,204] Fig. 19(a) shows perovskite dimensionality of a 2D perovskite structure (n = 1, 2...) and a 3D perovskite structure (n = N).[204] Compared with a 3D perovskite, the most distinguished advantage of 2D materials is an improved stability. A long and bulkier hydrophobic organic spacer (RNH_3^+) such as phenylethylammonium (PEA) or butylammonium (BA) can protect the perovskite from moisture. Stability is better with a lower n value. Tsai *et al.*[205] prepared a n-butylamine (BA, $C_4H_9NH_3$)-based 2D $(BA)_2(MA)_3Pb_4I_{13}$ perovskite by a hot casting method and obtained a high PCE of 12.5%. With this method, the perovskite crystal orientation was well-controlled along the out-of-plane direction which facilitates the charge transport as shown in Fig. 19(b). Compared to its 3D counterparts, the 2D perovskite solar cells show greater photo stability and humidity tolerance (Fig. 19(c)). So far, the highest PCE of 2D perovskite solar cells based on a low n value is only 14.1%, which was obtained by a quasi-2D $(PEA)_2(MA)_4Pb_5I_{16}$ (n = 5) perovskite with preferential orientation as a light harvester.[206] This PCE is still lags much farther behind those of 3D perovskites due to an improper band gap or absorption coefficient. Therefore, it is of significant

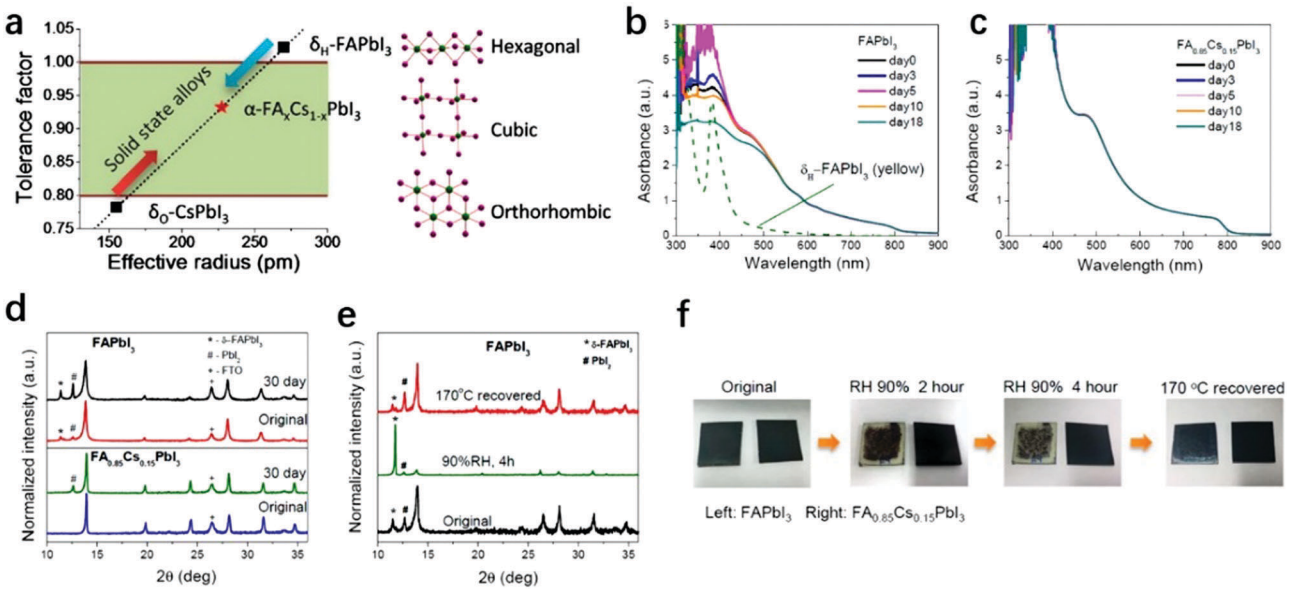

Fig. 18 (a) Schematic illustration of the tolerance factor with the A cation size and corresponding phase properties. Stability of $FAPbI_3$ and $FA_{0.85}Cs_{0.15}PbI_3$ films: UV-Vis spectra changes of (b) $FAPbI_3$ and (c) $FA_{0.85}Cs_{0.15}PbI_3$ after 18 days. (d) XRD pattern of $FAPbI_3$ and $FA_{0.85}Cs_{0.15}PbI_3$ films after storage for 30 days. (e) XRD change of $FAPbI_3$ thin film after being exposed to high humidity, and (f) photos of $FAPbI_3$ and $FA_{0.85}Cs_{0.15}PbI_3$ thin films under high-humidity conditions. Reproduced with permission from ref. 54. Copyright 2015, American Chemical Society.

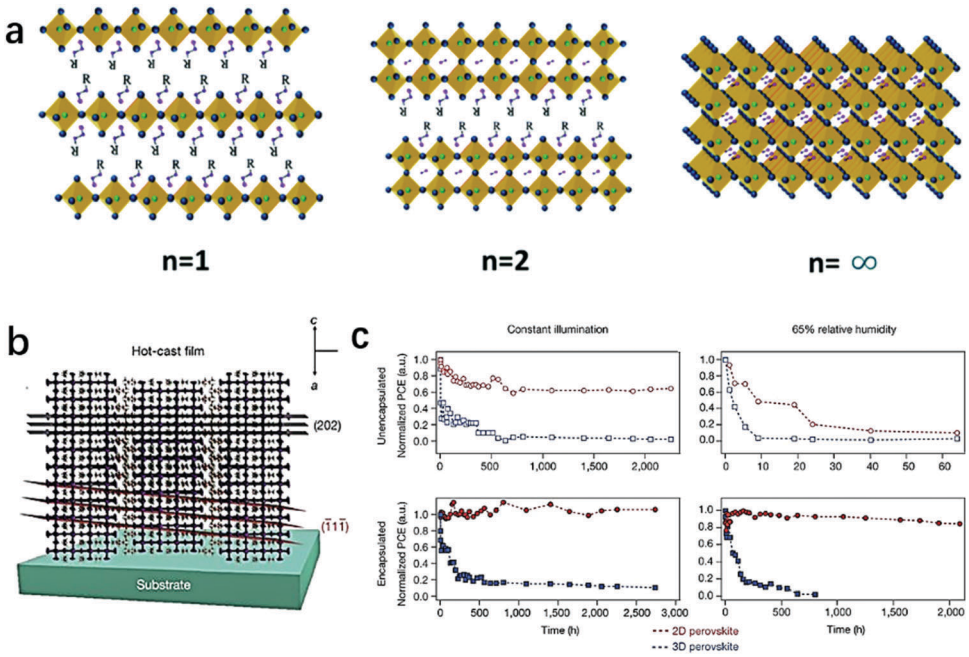

Fig. 19 (a) A scheme showing evolution of the perovskite dimensionality from n = 1 and n = 2 for a 2D perovskite structure, to n = N for a 3D perovskite structure. R represents a carbon chain. Reproduced with permission from ref. 204. Copyright 2018, The Royal Society of Chemistry. (b) Schematic representation of the (101) orientation along with the (111) and (202) planes of a 2D perovskite crystal. (c) Photo stability tests and humidity stability tests for 2D ($(BA)_2(MA)_3Pb_4I_{13}$; red) and 3D ($MAPbI_3$; blue) perovskite devices without and with encapsulation. Reproduced with permission from ref. 205. Copyright 2016, Springer Nature.

importance to control the layered perovskite crystal orientation to achieve an optimal balance of stability and efficiency.

The encapsulation technique provided an effective solution to circumvent environmental instability.[194,207] Cheacharoen *et al.*[191] demonstrated that the softer ethylene vinyl acetate encapsulated solar cells maintained over 90% of their initial performance at 85 °C after 200 cycles. Post treatment methods, such as surface modification, interface structure engineering, and hydrophobic additives blending into a perovskite can effectively enhance stability.[208–210] Li *et al.* applied a 2-aminoethanethiol (2-AET) ligand for the preparation of a $MAPbI_3$ perovskite film.[211] As shown in Fig. 20(a), the resulting $MAPbI_3$ perovskite crystal structure was retained for almost 10 minutes in water. As schematic diagram of the degradation process in Fig. 20(b) and (c) shows that the significantly enhanced water-resistance was due to the formation of water-resistant $MAPbI_3{\cdot}(x)_2$-AET perovskite. This work shed light on long-term stable $MAPbI_3$ perovskite devices.

The device architecture, selective contact layers, and metal electrode also exert large effects on the stability of PSCs.

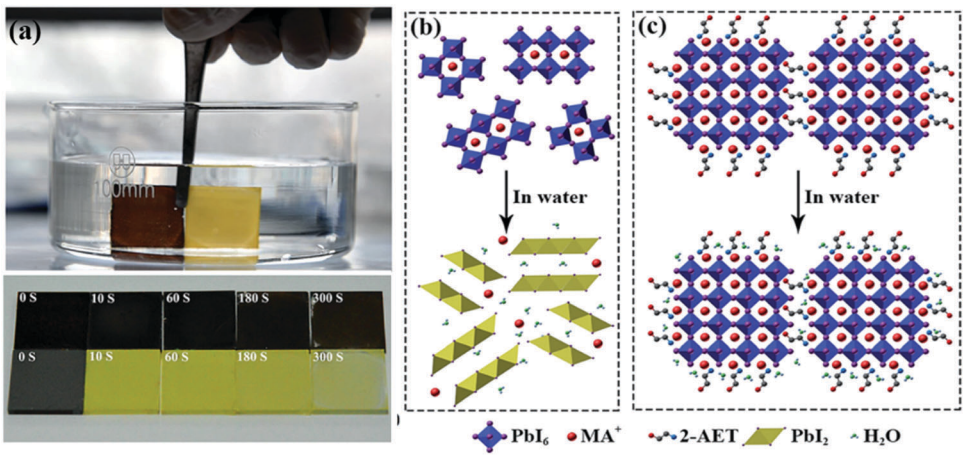

Fig. 20 (a) Photographs of $MAPbI_3{\cdot}(0.5)2$-AET (top) and $MAPbI_3$ (bottom) perovskite films immersed in water at different times. (b) The degradation process of $MAPbI_3$ and (c) mechanisms for water-resistant $MAPbI_3{\cdot}(x)_2$-AET perovskite in water. Reproduced with permission from ref. 211 Copyright 2016, The Royal Society of Chemistry.

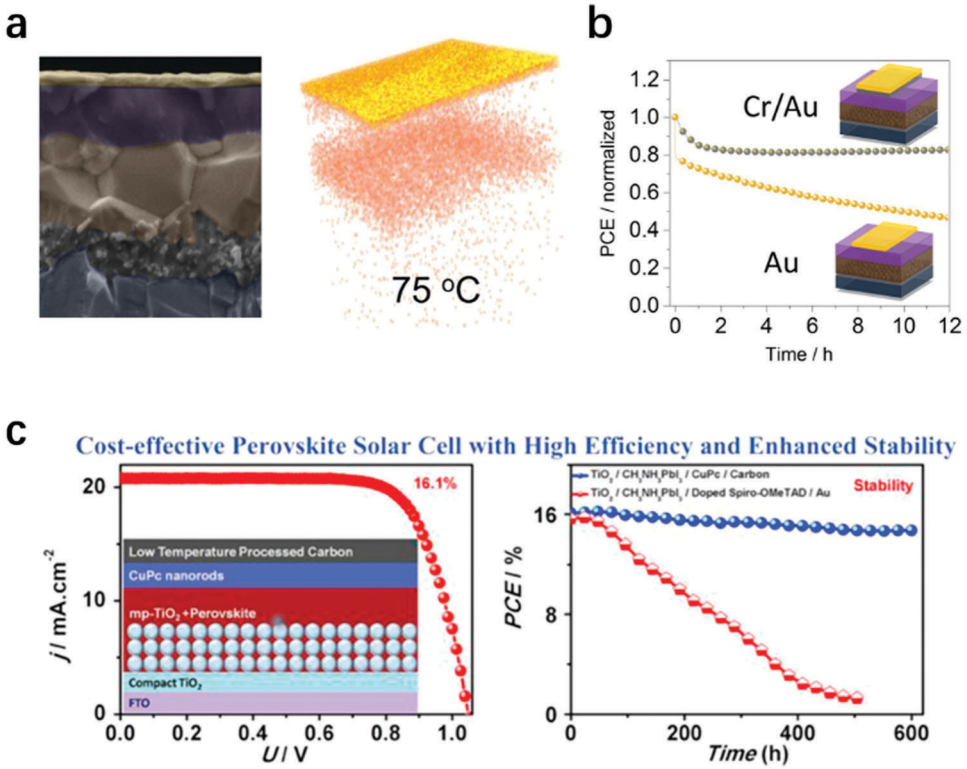

Fig. 21 (a) Cross-sectional SEM image of a perovskite solar cell and reconstructed 3D maps of the Au elements at 75 °C measured with ToF-SIMS. (b) Normalized PCE of a solar cell with an Au or Cr/Au electrode. Reproduced with permission from ref. 216, Copyright 2016, American Chemical Society. (c) The solar cell architecture, *J*–*V* curves, and stability performance of PSCs with CuPc nanorods as hole transport material and carbon as a counter electrode. Reproduced with permission from ref. 219, Copyright 2016, Elsevier.

The most effective PSCs are obtained using p-type organic semiconductors as hole transfer materials, such as 2,2′,7,7′-tetrakis-(*N*,*N*-di-*p*-methoxyphenylamine)-9,9′-spiro-bifluorene (spiro-OMeTAD) and polytriarylamine (PTAA). However, the 4-*tert*-butylpyridine or organic lithium salt additives in spiro-OMeTAD can diffuse into the perovskite and organic lithium salts absorb water easily. All these factors can accelerate a device's degradation.[212] Constructing all-inorganic contacts (TiO_2–CuSCN, NiO_x–ZnO, *etc.*) was demonstrated as a promising way to improve device stability.[11,213,214] In addition to the selective contact layers, metal electrodes are easy to form metal halides which are resistive and their usage would introduce iodide deficiency to a perovskite.[215–217] Although Au is less reactive than Ag or Al, it still can diffuse through a perovskite and the most wildly used hole transfer material spiro-OMeTAD is shown in Fig. 21(a).[216] To solve this problem, Fig. 21(b) shows that a Cr/Au electrode can slow the diffusion or reaction of Au with iodide.[216] Cu was also used as an electrode to replace Au.[218] However, these methods cannot solve the underlying problem. Other materials as electrodes and hole transport layers have been applied to improve PSC stability. For example, Sun *et al.*[219] applied CuPc nanorods hole transport material and a carbon counter electrode to obtain low cost PSCs with good stability (Fig. 21(c)).

The formation process of a perovskite crystal is also influenced by ambient conditions. When manufacturing perovskite films, typically a glove box is necessary to guarantee low humidity during the fabrication process although it was reported that a small amount of water present in an organic halide precursor solution helps with the grain growth of perovskite thin films.[220,221] The presence of water considerably accelerates the degradation of perovskite solar cells so tight control of humidity is necessary to ensure the stability of PSCs.

5.2 Toxicity

So far, PSCs with the best performance were achieved with a lead-based perovskite. However, lead presents a great threat to human health and safety of the entire ecosystem. Lead toxicity is considered as one of the challenges facing the PSC industry.[31,39,222] Due to the instability of perovskites, it's easy to decompose them into a moderately water-soluble carcinogen (PbI_2) in a humid environment or under strong UV radiation. Notably, the decomposition procedure is irreversible.[223–225] Although proper encapsulation of a device can effectively control the lead toxicity, it also will increase the device's cost. There are lead-based PSCs still in compliance with the strict environmental regulations in the marketplace.[226] Therefore, low-toxicity perovskite materials for PSCs have attracted much attention. The most effective method is total substitution of lead with low toxicity elements such as Sn, Bi, Sb, and Cu, *etc.*[227–231]

A Sn-based halide perovskite ($MASnX_3$, X = Cl, Br, I) is considered as the most promising non-toxic material for perovskites. Fig. 22(a) shows the crystal structure of tetragonal

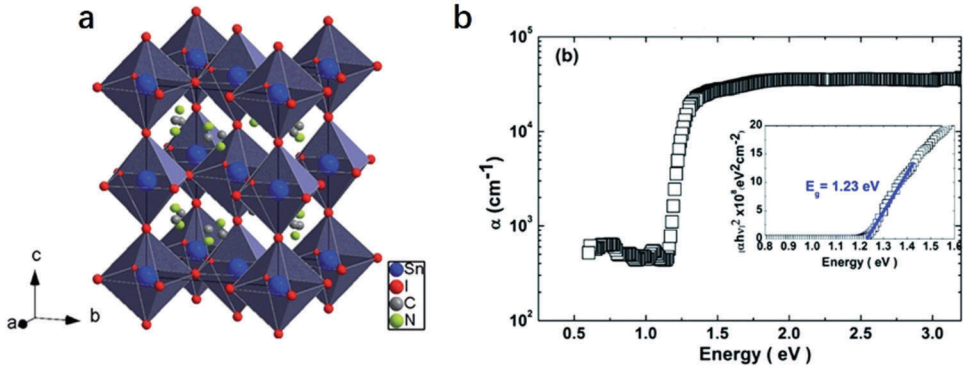

Fig. 22 (a) Crystal structure of tetragonal $CH_3NH_3SnI_3$ perovskite. (b) Light-absorption spectrum of $CH_3NH_3SnI_3$ with optical bandgap derived from a Tauc plot (inset image). Reproduced with permission from ref. 232. Copyright 2014, RSC.

$CH_3NH_3SnI_3$ perovskite, which is similar to the lead-based perovskite. It has a narrow direct optical band-gap of 1.23 eV, as shown in Fig. 22(b).[232] The biggest problem for a Sn-based halide perovskite is that divalent Sn^{2+} is very easy to be oxidized into the more stable Sn^{4+}, leading to high level of Sn^{4+} doping in Sn-based perovskite films and Sn vacancies. This will cause severe charge recombination in PSCs.[233] Efforts have been made to suppress charge recombination, for example, SnF_2 was introduced to suppress oxidation of Sn^{2+} and to fill tin vacancies.[234] However, the concentration of SnF_2 is difficult to control and an excess of SnF_2 can lead to the reduction of device performance. The PCEs of Sn-based low toxic perovskite solar cells still lag far behind Pb-based perovskite solar cells. To enhance the performance and stability of Sn-based perovskites,

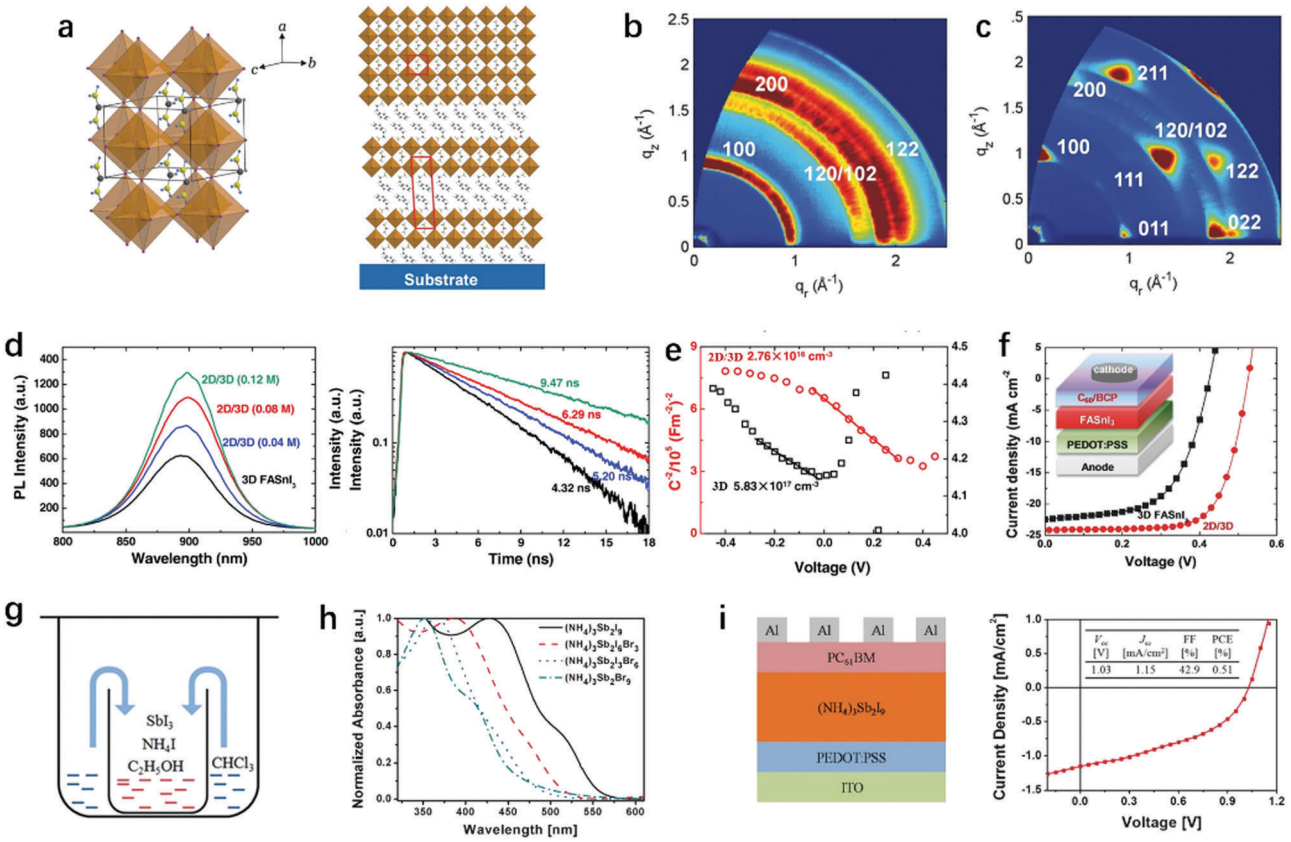

Fig. 23 Schematic illustration of the crystal structures of (a) 3D and 2D/3D mixed $FAPbI_3$ perovskite. GIWAXS images of the (b) 3D and (c) 2D/3D mixed $FAPbI_3$ perovskite samples at an incident angle of 0.25. (d) Steady state PL and time-resolved PL spectra of different samples. (e) Variation of the background charge carrier density of 3D and 2D/3D mixed $FAPbI_3$ perovskite devices. (f) J–V curves for the champion 3D and 2D/3D mixed $FAPbI_3$ perovskite devices. Reproduced with permission from ref. 235. Copyright 2018, Wiley. (g) Diagram illustrating the preparation approach for $(NH_4)_3Sb_2I_9$ single crystals. (h) Absorption spectra for $(NH_4)_3Sb_2I_xBr_{9-x}$ films. (i) The device structure and J–V curve for the $(NH_4)_3Sb_2I_9$ solar cell. Reproduced with permission from ref. 236, Copyright 2017, Wiley.

highly crystalline 2D/3D mixed $FASnI_3$ perovskite films were fabricated by mixing 0.08 M 2D $PEA_2FA_{n+1}S_nI_{3n+1}$ with 0.92 M 3D $FASnI_3$.[235] Fig. 23(a)–(c) give the crystal structure of a 3D $FASnI_3$ and 2D/3D mixture (2D 0.08 M) as well as the GIWAX images, respectively. Compared with the 3D $FASnI_3$ perovskite film, 3D grains of the mixed perovskite films show well-defined orientation and superior crystallinity. The steady-state PL and time-resolved PL spectra and the background charge carrier density of the samples in Fig. 23(d) and (e) show that the mixed perovskite displays low recombination losses of charge carriers. As a result, the best PCE of PSCs based on a 2D/3D mixed $FASnI_3$ perovskite reached 9% with negligible hysteresis, which was the highest value for Sn-based non-toxicity PSCs.[235]

Other non-toxic perovskites also have been developed. For example, Zuo *et al.*[236] reported a family of novel lead-free perovskites, $(NH_4)_3Sb_2I_xBr_{9-x}$ ($0 < x < 9$). These materials were prepared with ethanol, an eco-friendly solvent due to good solubility in it of SbI_3 and NH_4I (Fig. 23(g)). The absorption onset of $(NH_4)_3Sb_2I_xBr_{9-x}$ films range from 558 nm to 453 nm, as shown in Fig. 23(h). The prepared $(NH_4)_3Sb_2I_9$ perovskites are single crystals with a hole mobility of 4.8 $cm^2\ V^{-1}\ s^{-1}$ and an electron mobility of 12.3 $cm^2\ V^{-1}\ s^{-1}$. The solar cells based on these materials generated an open-circuit voltage of 1.03 V and a PCE of 0.51%, as shown in Fig. 23(i). This work indicates that there are still many opportunities to enrich the non-toxicity perovskite family. In 2018, Jiang *et al.*[237] demonstrated that methylammonium Sb halide perovskites $(CH_3NH_3)_3Sb_2Cl_xI_{9-x}$ with Cl incorporation as efficient light absorbers show over 2% PCE for non-toxic perovskite solar cells.

Scalable manufacturing is usually proceeded under environmental conditions. Accordingly, priority should be given the to address toxicity issues during the fabrication process, *e.g.*, operators should avoid direct contact with volatile organic solvents. Considering solvating power, the choice of a solvent is limited by the coordination interaction between solvent and inorganic component. At present, the most frequently used solvent to prepare a perovskite precursor solution is DMF but other solvents of first choice include GBL or a mixture of GBL with DMSO.[95,238] Unfortunately, those solvents are toxic, which is an inevitable barrier to large-scale production. Developing a new green nonhazardous solvent system is required to achieve safe fabrications. Gardner and co-workers developed a nonhazardous solvent system with a mixture of γ-butyrolactone, ethanol, and acetic acid to prepare a perovskite precursor; the efficiency of these produced PSCs which achieved a PCE of 15.1%.[93] Acetonitrile (ACE) was also reported to replace highly coordinated and toxic solvents. Despite that inorganic compounds were insoluble in ACE, the introduction of methylamine improved the solvating power of ACE to obtain a perovskite precursor lacking strong toxicity and yielding an impressive PCE of 19%.[94] New materials with outstanding physical properties through low-cost and environmental friendly synthesis and processing routes may be the most effective way to avoid physical ailments to the operator or user.

5.3 Module cost

Earth-abundant raw materials and compatibility with various low temperature and cost-efficient solution-processing fabrication

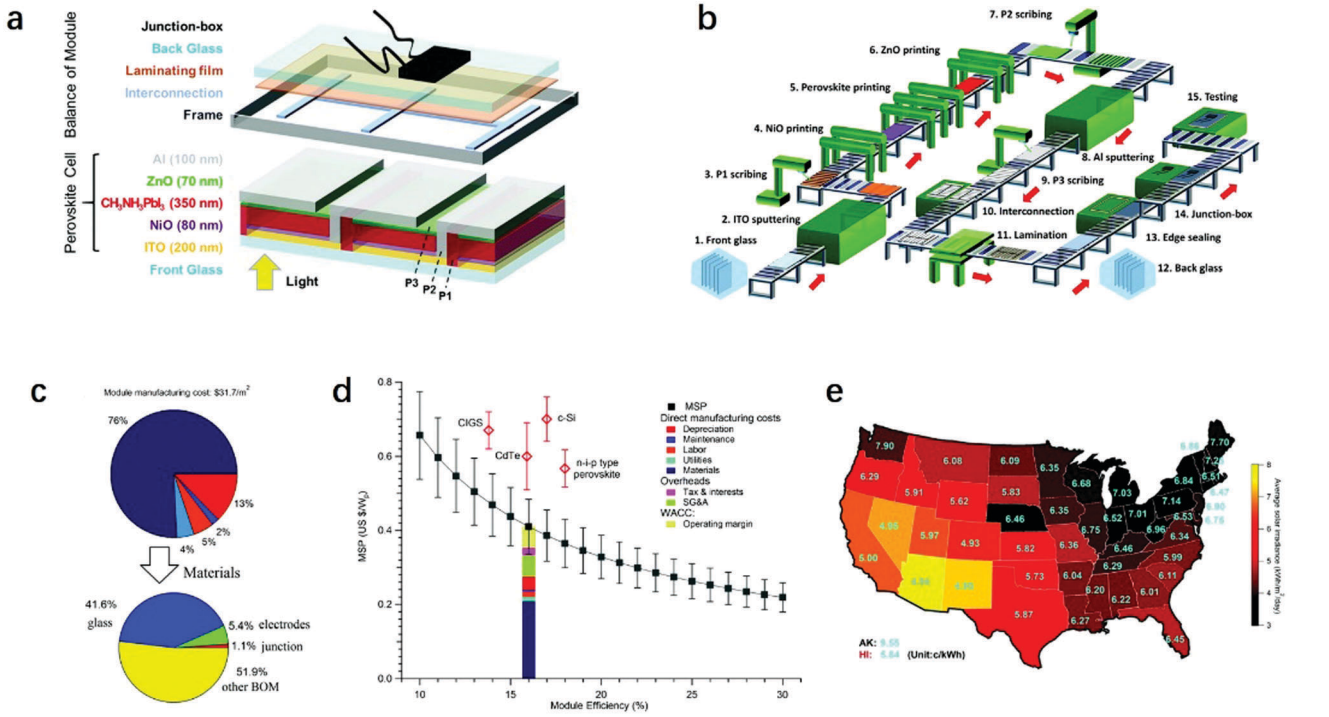

Fig. 24 (a and b) The reference perovskite module and selected manufacturing process. (c) The direct manufacturing cost for a perovskite module manufactured in US. (d) Minimum sustainable price (MSP) as a function of module efficiency. (e) Average solar irradiation and the estimated levelized cost of energy (LCOE) values in the US. Reproduced with permission from ref. 242, Copyright 2017, Elsevier.

methods make PSCs a promising competitor with Si and CIGS solar cells for commercialization. Commercialization of PSCs is an unstoppable trend. It is important to evaluate a perovskite module's cost. Several research groups have assessed the cost for manufacturing perovskite modules based on different device structures and manufacturing processes.[239–243] Song *et al.*[242] performed a much more complete assessment of the cost of PSC modules. Fig. 24(a) and (b) show a reference perovskite module and selected manufacturing processes. With careful assessment of each module's processing process, direct manufacturing cost for a perovskite module manufactured in US was about \$\$31.7 per m^2 (Fig. 24(c)). Assuming modules operate at 16% PCE, the minimum sustainable price (MSP) is about \$\$0.41 per Wp (Fig. 24(d)). Fig. 24(e) shows that the levelized cost of energy (LCOE) values is in the range of 4.93 to 7.90¢ per KW per h in USA for perovskite solar module with a PCE of 16%. This result shows that a perovskite PV may be more cost-effective than c-Si and thin-film CdTe modules. Reducing degradation and increasing PCE would further reduce module cost. If the stability and long-term lifetime issues can be resolved, then the cost for PSC modules manufacturing will be even lower.

6. Concluding remarks and outlook

Owing to the intrinsic broad optical absorption, high charge carrier mobility, low exciton binding energy, and long free carrier diffusion length of organic–inorganic hybrid perovskites as well as their low-cost solution manufacture, PSCs have become a strong contender in the photovoltaic market, rivaling the widely successful silicon-based solar cells and the mature thin-film cadmium telluride (CdTe) and copper indium gallium selenide (CIGS) solar cells. The PCEs of PSCs has advanced from 3.8% to 22.7% in laboratory scale in less than a decade, which has laid a solid foundation and motivated the photovoltaic communities' efforts to promote its commercialization. Owing to the low activation energy of perovskites, nucleation and subsequent crystal growth are readily occurring at room temperature during solution processes. Such a low activation energy also leads to a very rapid nucleation and crystal growth process and allows significant influences from subtle changes of other processing parameters including temperature, pressure, additives, impurities, solvents, and types of precursors, which at least partially explain the fact that power conversion efficiency varies widely from one research group to another even following the same synthesis procedure and parameters.

Extensive research with laboratory scale solar cell devices has revealed the fact that power conversion efficiency, hysteresis, and stability of PSCs are largely dependent on the quality of perovskite crystals including the crystallinity or the degree of perfection, morphology, and interfaces. Such ample knowledge and experience have laid a solid foundation for further exploration and development of a range of large-scale solution fabrication processes for commercialization. It is imperative to develop scalable fabrication technologies capable of retaining the ability of nucleation and subsequently crystal growth processes and control of the processing environment and parameters. Solution fabrication processes directly inherit many advantages and similarities from lab-scale fabrication processes. Some generic considerations and requirements include:

(1) Promoting heterogeneous nucleation at the interface, preferably at the solid-solution interface, with subsequent oriented growth across the perovskite films, *i.e.*, preventing homogeneous and secondary nucleation, to obtain a "single crystal" film across the film.

(2) Keeping the nucleation density low so that each crystallite grows to several or tens of micrometers in lateral dimension so there will be a small number of grain boundaries.

(3) Ensuring the crystal growth proceeds in a near thermodynamic equilibrium condition to achieve very high crystal perfection with minimal defects or impurities.

(4) Developing an effective annealing process similar to the "Bridgman–Stockbarger technique," or simply the Bridgman technique to convert a polycrystalline film to a single crystal film or to improve crystallinity and remove defects from perovskite films.

(5) Improving interface and surface properties. It has been very clear that PSC performance is largely affected by interface and surface properties, second to the quality of perovskite films, to achieve a desired surface/interface chemistry, coherency, and passivation.

(6) Developing reliable equipment and precursor solutions to realize the scalable fabrication of every layer in a PSC.

(7) Developing a fabrication process less sensitive to the fabrication environment and parameters including temperature, vapor pressure, and solvent, impurities/additives.

At present, there are still many challenges for the commercialization of PSCs (such as low PCE of large-area devices, lack of long-term stability, and high toxicity of some solvents). To seek scalable fabrications that are low-cost, environmentally-friendly, have high stock utilization, and PCEs supporting commercialization is still the focus of perovskite solar cell studies. Furthermore, more attention should be paid to new materials with outstanding physical properties through development of low-cost and environmentally friendly synthesis and processing routes. Packaging techniques for applying a water-resistant layer on the surface of perovskite solar cells may provide solutions to circumvent environmental instability as well. In addition, crystal crosslinking with modified molecules, or hydrophobic additives blending into a perovskite, also will improve stability towards commercialization.

Conflicts of interest

There are no conflicts to declare.

Acknowledgements

This work was supported by the National Key Research and Development Program (2017YFE0119700), National Natural Science Foundation of China (51774034, 51772026 and 51611130063),

Beijing Natural Science Foundation (2182039), the Slovak Research and Development Agency, project APVV (SK-CN-RD-18-0006), Fundamental Research Funds for the Central Universities (FRF-TP-17-030A1, FRF-TP-17-083A1, FRF-TP-17-082A1, TW2018010), and Project funded by China Postdoctoral Science Foundation (2017M620611, 2018M630068).

References

1 H. J. Snaith, *Nat. Mater.*, 2018, **17**, 372–376.
2 J. Huang, Y. Yuan, Y. Shao and Y. Yan, *Nat. Rev. Mater.*, 2017, **2**, 17042.
3 A. Kojima, K. Teshima, Y. Shirai and T. Miyasaka, *J. Am. Chem. Soc.*, 2009, **131**, 6050–6051.
4 NREL, Efficiency chart,http://www.nrel.gov/pv/assets/images/efficiency-chart-20190716.
5 A. Priyadarshi, L. J. Haur, P. Murray, D. Fu, S. Kulkarni, G. Xing, T. C. Sum, N. Mathews and S. G. Mhaisalkar, *Energy Environ. Sci.*, 2016, **9**, 3687–3692.
6 M. Yang, Z. Li, M. O. Reese, O. G. Reid, D. H. Kim, S. Siol, T. R. Klein, Y. Yan, J. J. Berry and M. F. van Hest, *Nat. Energy*, 2017, **2**, 17038.
7 M. Yang, D. H. Kim, T. R. Klein, Z. Li, M. O. Reese, B. J. Tremolet de Villers, J. J. Berry, M. F. van Hest and K. Zhu, *ACS Energy Lett.*, 2018, **3**, 322–328.
8 J. M. Ball, S. D. Stranks, M. T. Hörantner, S. Hüttner, W. Zhang, E. J. Crossland, I. Ramirez, M. Riede, M. B. Johnston and R. H. Friend, *Energy Environ. Sci.*, 2015, **8**, 602–609.
9 M. A. Green, Y. Hishikawa, E. D. Dunlop, D. H. Levi, J. Hohl-Ebinger and A. W. Ho-Baillie, *Prog. Photovolt.: Res. Appl.*, 2018, **26**, 3–12.
10 N. J. Jeon, J. H. Noh, W. S. Yang, Y. C. Kim, S. Ryu, J. Seo and S. I. Seok, *Nature*, 2015, **517**, 476–480.
11 N. Arora, M. I. Dar, A. Hinderhofer, N. Pellet, F. Schreiber, S. M. Zakeeruddin and M. Gratzel, *Science*, 2017, **358**, 768–771.
12 D.-Y. Son, J.-W. Lee, Y. J. Choi, I.-H. Jang, S. Lee, P. J. Yoo, H. Shin, N. Ahn, M. Choi, D. Kim and N.-G. Park, *Nat. Energy*, 2016, **1**, 16081.
13 J.-P. Correa-Baena, W. Tress, K. Domanski, E. H. Anaraki, S.-H. Turren-Cruz, B. Roose, P. P. Boix, M. Grätzel, M. Saliba, A. Abate and A. Hagfeldt, *Energy Environ. Sci.*, 2017, **10**, 1207–1212.
14 G. Niu, W. Li, J. Li and L. Wang, *Sci. China Mater.*, 2016, **59**, 728–742.
15 D. Yang, R. Yang, K. Wang, C. Wu, X. Zhu, J. Feng, X. Ren, G. Fang, S. Priya and S. F. Liu, *Nat. Commun.*, 2018, **9**, 3239.
16 W. Nie, H. Tsai, J. C. Blancon, F. Liu, C. C. Stoumpos, B. Traore, M. Kepenekian, O. Durand, C. Katan and S. Tretiak, *Adv. Mater.*, 2018, **30**, 1703879.
17 D. T. Moore, H. Sai, K. W. Tan, D. M. Smilgies, W. Zhang, H. J. Snaith, U. Wiesner and L. A. Estroff, *J. Am. Chem. Soc.*, 2015, **137**, 2350–2358.
18 U. Köster, *Phys. Status Solidi B*, 1978, **48**, 313–321.
19 Y. Deng, E. Peng, Y. Shao, Z. Xiao, Q. Dong and J. Huang, *Energy Environ. Sci.*, 2015, **8**, 1544–1550.
20 K. Hwang, Y. S. Jung, Y. J. Heo, F. H. Scholes, S. E. Watkins, J. Subbiah, D. J. Jones, D. Y. Kim and D. Vak, *Adv. Mater.*, 2015, **27**, 1241–1247.
21 P. Li, C. Liang, B. Bao, Y. Li, X. Hu, Y. Wang, Y. Zhang, F. Li, G. Shao and Y. Song, *Nano Energy*, 2018, **46**, 203–211.
22 Mark Hutchins, Oxford PV picks up GBP 8.02 million in investments [N]. PV Magazine Internationals, 2018, vol. 4, p. 24.
23 Mark Hutchins, Oxford PV hits world record efficiency for perovskite/silicon tandem cell PV [N] Magazine Internationals, 2018, vol. 6, p. 26.
24 Solaronix, Solaronix achieves major breakthrough toward perovskite solar cell industrialization [N]. PV Magzine International, 2016, vol. 7, p. 13.
25 S. G. Hashmi, D. Martineau, M. I. Dar, T. T. Myllymäki, T. Sarikka, V. Ulla, S. M. Zakeeruddin and M. Grätzel, *J. Mater. Chem. A*, 2017, **5**, 12060–12067.
26 G. Grancini, C. Roldan-Carmona, I. Zimmermann, E. Mosconi, X. Lee, D. Martineau, S. Narbey, F. Oswald, F. De Angelis, M. Graetzel and M. K. Nazeeruddin, *Nat. Commun.*, 2017, **8**, 15684.
27 The OSA director news letter: http://www.osadirect.com/news/article/2154/greatcell-solar-has-receives-eu-horizon-2020-project-award-of-500000/.
28 https://www.toshiba.co.jp/rdc/rd/detail_e/e1709_02.html.
29 https://www.perovskite-info.com/microquanta-reaches-179-perovskite-solar-mini-module.
30 F. Lang, O. Shargaieva, V. V. Brus, H. C. Neitzert, J. Rappich and N. H. Nickel, *Adv. Mater.*, 2017, **30**, 1702905.
31 M. Gratzel, *Nat. Mater.*, 2014, **13**, 838–842.
32 A. Babayigit, A. Ethirajan, M. Muller and B. Conings, *Nat. Mater.*, 2016, **15**, 247–251.
33 L. K. Ono, N.-G. Park, K. Zhu, W. Huang and Y. Qi, *ACS Energy Lett.*, 2017, **2**, 1749–1751.
34 M. Saliba, J.-P. Correa-Baena, M. Graetzel, A. Hagfeldt and A. Abate, *Angew. Chem., Int. Ed.*, 2017, **57**, 2554–2569.
35 J. Bisquert, Y. Qi, T. Ma and Y. Yan, *ACS Energy Lett.*, 2017, **2**, 520–523.
36 Q. Han, Y. Bai, J. Liu, K.-z. Du, T. Li, D. Ji, Y. Zhou, C. Cao, D. Shin, J. Ding, A. D. Franklin, J. T. Glass, J. Hu, M. J. Therien, J. Liu and D. B. Mitzi, *Energy Environ. Sci.*, 2017, **10**, 2365–2371.
37 E. M. Hutter, J.-J. Hofman, M. L. Petrus, M. Moes, R. D. Abellón, P. Docampo and T. J. Savenije, *Adv. Energy Mater.*, 2017, **7**, 1602349.
38 Z. Wang, Z. Shi, T. Li, Y. Chen and W. Huang, *Angew. Chem., Int. Ed.*, 2016, **56**, 1190–1212.
39 F. Hao, C. C. Stoumpos, D. H. Cao, R. P. H. Chang and M. G. Kanatzidis, *Nat. Photonics*, 2014, **8**, 489–494.
40 L. Guo, C. Fei, R. Zhang, B. Li, T. Shen, J. Tian and G. Cao, *Sci. China Mater.*, 2016, **59**, 710–718.
41 M. M. Tavakoli, S. M. Zakeeruddin, M. Grätzel and Z. Fan, *Adv. Mater.*, 2018, **30**, 1705998.

42 R. Zhou, Z. Yang, J. Xu and G. Cao, *Coord. Chem. Rev.*, 2018, **374**, 279–313.
43 Y. Rong, Y. Ming, W. Ji, D. Li, A. Mei, Y. Hu and H. Han, *J. Phys. Chem. Lett.*, 2018, **9**, 2707–2713.
44 Y.-S. Jung, K. Hwang, Y.-J. Heo, J.-E. Kim, D. Vak and D.-Y. Kim, *Adv. Opt. Mater.*, 2018, **6**, 1701182.
45 S. Razza, S. Castro-Hermosa, A. Di Carlo and T. M. Brown, *APL Mater.*, 2016, **4**, 091508.
46 S. T. Williams, A. Rajagopal, C.-C. Chueh and A. K.-Y. Jen, *J. Phys. Chem. Lett.*, 2016, **7**, 811–819.
47 J. Wei, C. Shi, Y. Zhao, W. Zhou, H. Li, R. Fu, D. Yu and Q. Zhao, *Sci. China Mater.*, 2016, **59**, 769–778.
48 D. Angmo, M. Gao and D. Vak, *Printable Sol. Cells*, 2017, 313–362.
49 Z. Li, T. R. Klein, D. H. Kim, M. Yang, J. J. Berry, M. F. A. M. van Hest and K. Zhu, *Nat. Rev. Mater.*, 2018, **3**, 18017.
50 N.-G. Park, *Mater. Today*, 2015, **18**, 65–72.
51 D. T. Moore, H. Sai, K. W. Tan, D.-M. Smilgies, W. Zhang, H. J. Snaith, U. Wiesner and L. A. Estroff, *J. Am. Chem. Soc.*, 2015, **137**, 2350–2358.
52 A. Poglitsch and D. Weber, *J. Chem. Phys.*, 1987, **87**, 6373–6378.
53 J. Even, L. Pedesseau, J. M. Jancu and C. Katan, *Phys. Status Solidi RRL*, 2014, **8**, 31–35.
54 Z. Li, M. Yang, J.-S. Park, S.-H. Wei, J. J. Berry and K. Zhu, *Chem. Mater.*, 2015, **28**, 284–292.
55 V. M. Goldschmidt, *Naturwissenschaften*, 1926, **14**, 477–485.
56 W. Travis, E. Glover, H. Bronstein, D. Scanlon and R. Palgrave, *Chem. Sci.*, 2016, **7**, 4548–4556.
57 D. B. Mitzi, *Prog. Inorg. Chem.*, 1999, 1–121.
58 E. L. Da Silva, J. M. Skelton, S. C. Parker and A. Walsh, *Phys. Rev. B: Condens. Matter Mater. Phys.*, 2015, **91**, 144107.
59 Q. Wang, Y. Shao, Q. Dong, Z. Xiao, Y. Yuan and J. Huang, *Energy Environ. Sci.*, 2014, **7**, 2359–2365.
60 C. Li, X. Lu, W. Ding, L. Feng, Y. Gao and Z. Guo, *Acta Crystallogr., Sect. B: Struct. Sci.*, 2008, **64**, 702–707.
61 Q. Dong, Y. Fang, Y. Shao, P. Mulligan, J. Qiu, L. Cao and J. Huang, *Science*, 2015, **347**, 967–970.
62 D. Shi, V. Adinolfi, R. Comin, M. Yuan, E. Alarousu, A. Buin, Y. Chen, S. Hoogland, A. Rothenberger and K. Katsiev, *Science*, 2015, **347**, 519–522.
63 T. M. Brenner, D. A. Egger, A. M. Rappe, L. Kronik, G. Hodes and D. Cahen, *J. Phys. Chem. Lett.*, 2015, **6**, 4754–4757.
64 G. Xing, N. Mathews, S. Sun, S. S. Lim, Y. M. Lam, M. Gratzel, S. Mhaisalkar and T. C. Sum, *Science*, 2013, **342**, 344–347.
65 S. D. Stranks, G. E. Eperon, G. Grancini, C. Menelaou, M. J. Alcocer, T. Leijtens, L. M. Herz, A. Petrozza and H. J. Snaith, *Science*, 2013, **342**, 341–344.
66 Z. Xiao, Q. Dong, C. Bi, Y. Shao, Y. Yuan and J. Huang, *Adv. Mater.*, 2014, **26**, 6503–6509.
67 Z. Fan, K. Sun and J. Wang, *J. Mater. Chem. A*, 2015, **3**, 18809–18828.
68 G. Xing, N. Mathews, S. Sun, S. S. Lim, Y. M. Lam, M. Grätzel, S. Mhaisalkar and T. C. Sum, *Science*, 2013, **342**, 344–347.
69 S. De Wolf, J. Holovsky, S.-J. Moon, P. Löper, B. Niesen, M. Ledinsky, F.-J. Haug, J.-H. Yum and C. Ballif, *J. Phys. Chem. Lett.*, 2014, **5**, 1035–1039.
70 N. Jensen, R. Hausner, R. Bergmann, J. Werner and U. Rau, *Prog. Photovolt.: Res. Appl.*, 2002, **10**, 1–13.
71 N. C. Giebink, G. P. Wiederrecht, M. R. Wasielewski and S. R. Forrest, *Phys. Rev. B: Condens. Matter Mater. Phys.*, 2011, **83**, 195326.
72 V. D'Innocenzo, G. Grancini, M. J. Alcocer, A. R. Kandada, S. D. Stranks, M. M. Lee, G. Lanzani, H. J. Snaith and A. Petrozza, *Nat. Commun.*, 2014, **5**, 3586.
73 M. Hirasawa, T. Ishihara, T. Goto, K. Uchida and N. Miura, *Physica B*, 1994, **201**, 427–430.
74 A. Miyata, A. Mitioglu, P. Plochocka, O. Portugall, J. T.-W. Wang, S. D. Stranks, H. J. Snaith and R. J. Nicholas, *Nat. Phys.*, 2015, **11**, 582–587.
75 K. Tanaka, T. Takahashi, T. Ban, T. Kondo, K. Uchida and N. Miura, *Solid State Commun.*, 2003, **127**, 619–623.
76 M. Hu, C. Bi, Y. Yuan, Z. Xiao, Q. Dong, Y. Shao and J. Huang, *Small*, 2015, **11**, 2164–2169.
77 H. Chen, *Adv. Funct. Mater.*, 2017, **27**, 1605654.
78 J. Burschka, N. Pellet, S. J. Moon, R. Humphry-Baker, P. Gao, M. K. Nazeeruddin and M. Gratzel, *Nature*, 2013, **499**, 316–319.
79 Z. Xiao, C. Bi, Y. Shao, Q. Dong, Q. Wang, Y. Yuan, C. Wang, Y. Gao and J. Huang, *Energy Environ. Sci.*, 2014, **7**, 2619–2623.
80 W. S. Yang, B.-W. Park, E. H. Jung, N. J. Jeon, Y. C. Kim, D. U. Lee, S. S. Shin, J. Seo, E. K. Kim and J. H. Noh, *Science*, 2017, **356**, 1376–1379.
81 W. Yafei, L. Detao, Z. Peng, Z. Ting, A. Waseem, Y. Xiangxiao, W. Feng, L. Jian, C. Li and W. Jiang, *Sci. China Mater.*, 2018, **61**, 1536–1548.
82 A. R. Pascoe, Q. Gu, M. U. Rothmann, W. Li, Y. Zhang, A. D. Scully, X. Lin, L. Spiccia, U. Bach and Y.-B. Cheng, *Sci. China Mater.*, 2017, **60**, 617–628.
83 Y. Zhou, O. S. Game, S. Pang and N. P. Padture, *J. Phys. Chem. Lett.*, 2015, **6**, 4827–4839.
84 V. K. LaMer and R. H. Dinegar, *J. Am. Chem. Soc.*, 1950, **72**, 4847–4854.
85 G. Cao, *Nanostructures & nanomaterials: synthesis, properties & applications*, Imperial college press, 2004.
86 B. Ding, Y. Li, S.-Y. Huang, Q.-Q. Chu, C.-X. Li, C.-J. Li and G.-J. Yang, *J. Mater. Chem. A*, 2017, **5**, 6840–6848.
87 M. Haruta and B. Delmon, *J. Chim. Phys.*, 1986, **83**, 859–868.
88 S. Song, M. T. Hörantner, K. Choi, H. J. Snaith and T. Park, *J. Mater. Chem. A*, 2017, **5**, 3812–3818.
89 W. Nie, H. Tsai, R. Asadpour, J.-C. Blancon, A. J. Neukirch, G. Gupta, J. J. Crochet, M. Chhowalla, S. Tretiak, M. A. Alam, H.-L. Wang and A. D. Mohite, *Science*, 2015, **347**, 522–525.
90 S. Sanchez, X. Hua, N. Phung, U. Steiner and A. Abate, *Adv. Energy Mater.*, 2018, **12**, 1702915.
91 C. Zuo, D. Vak, D. Angmo, L. Ding and M. Gao, *Nano Energy*, 2018, **46**, 185–192.

92 T. Liu, Y. Zhou, Q. Hu, K. Chen, Y. Zhang, W. Yang, J. Wu, F. Ye, D. Luo and K. Zhu, *Sci. China Mater.*, 2017, **60**, 608–616.
93 K. L. Gardner, J. G. Tait, T. Merckx, W. Qiu, U. W. Paetzold, L. Kootstra, M. Jaysankar, R. Gehlhaar, D. Cheyns, P. Heremans and J. Poortmans, *Adv. Energy Mater.*, 2016, **6**, 1600386.
94 N. K. Noel, S. N. Habisreutinger, B. Wenger, M. T. Klug, M. T. Hörantner, M. B. Johnston, R. J. Nicholas, D. T. Moore and H. Snaith, *Energy Environ. Sci.*, 2011, **10**, 145–152.
95 N. J. Jeon, J. H. Noh, Y. C. Kim, W. S. Yang, S. Ryu and S. I. Seok, *Nat. Mater.*, 2014, **13**, 897.
96 K. Hendriks, J. J. van Franeker, B. J. Bruijnaers, J. A. Anta, M. M. Wienk and R. A. J. Janssen, *J. Mater. Chem. A*, 2017, **5**, 2346–2354.
97 Z. Arain, C. Liu, Y. Yang, M. Mateen, Y. Ren, Y. Ding, X. Liu, Z. Ali, M. Kumar and S. Dai, *Sci. China Mater.*, 2014, 1–12.
98 M. Xiao, F. Huang, W. Huang, Y. Dkhissi, Y. Zhu, J. Etheridge, A. Gray-Weale, U. Bach, Y. B. Cheng and L. Spiccia, *Angew. Chem.*, 2014, **126**, 10056–10061.
99 X. Li, D. Bi, C. Yi, J.-D. Décoppet, J. Luo, S. M. Zakeeruddin, A. Hagfeldt and M. Grätzel, *Science*, 2016, aaf8060.
100 L.-L. Gao, C.-X. Li, C.-J. Li and G.-J. Yang, *J. Mater. Chem. A*, 2017, **5**, 1548–1557.
101 F. Huang, Y. Dkhissi, W. Huang, M. Xiao, I. Benesperi, S. Rubanov, Y. Zhu, X. Lin, L. Jiang, Y. Zhou, A. Gray-Weale, J. Etheridge, C. R. McNeill, R. A. Caruso, U. Bach, L. Spiccia and Y.-B. Cheng, *Nano Energy*, 2014, **10**, 10–18.
102 L.-L. Gao, L.-S. Liang, X.-X. Song, B. Ding, G.-J. Yang, B. Fan, C.-X. Li and C.-J. Li, *J. Mater. Chem. A*, 2016, **4**, 3704–3710.
103 S. Razza, F. Di Giacomo, F. Matteocci, L. Cinà, A. L. Palma, S. Casaluci, P. Cameron, A. D'Epifanio, S. Licoccia, A. Reale, T. M. Brown and A. Di Carlo, *J. Power Sources*, 2015, **277**, 286–291.
104 L. Zhang, B. Li, J. Yuan, M. Wang, T. Shen, F. Huang, W. Wen, G. Cao and J. Tian, *J. Phys. Chem. Lett.*, 2018, **9**, 3646–3653.
105 K. Yan, M. Long, T. Zhang, Z. Wei, H. Chen, S. Yang and J. Xu, *J. Am. Chem. Soc.*, 2015, **137**, 4460–4468.
106 J. Borchert, R. L. Milot, J. B. Patel, C. L. Davies, A. D. Wright, L. Martínez Maestro, H. J. Snaith, L. M. Herz and M. B. Johnston, *ACS Energy Lett.*, 2017, **2**, 2799–2804.
107 M. Li, B. Li, G. Cao and J. Tian, *J. Mater. Chem. A*, 2017, **5**, 21313–21319.
108 B. Li, M. Li, C. Fei, G. Cao and J. Tian, *J. Mater. Chem. A*, 2017, **5**, 24168–24177.
109 H. Tsai, W. Nie, Y.-H. Lin, J. C. Blancon, S. Tretiak, J. Even, G. Gupta, P. M. Ajayan and A. D. Mohite, *Adv. Energy Mater.*, 2017, **7**, 1602159.
110 D. P. McMeekin, Z. Wang, W. Rehman, F. Pulvirenti, J. B. Patel, N. K. Noel, M. B. Johnston, S. R. Marder, L. M. Herz and H. J. Snaith, *Adv. Mater.*, 2017, **29**, 1607039.
111 C. Fei, B. Li, R. Zhang, H. Fu, J. Tian and G. Cao, *Adv. Energy Mater.*, 2016, **7**, 1602017.
112 D. W. de Quilettes, S. M. Vorpahl, S. D. Stranks, H. Nagaoka, G. E. Eperon, M. E. Ziffer, H. J. Snaith and D. S. Ginger, *Science*, 2015, **348**, 683–686.
113 Y. Shao, Y. Fang, T. Li, Q. Wang, Q. Dong, Y. Deng, Y. Yuan, H. Wei, M. Wang, A. Gruverman, J. Shield and J. Huang, *Energy Environ. Sci.*, 2016, **9**, 1752–1759.
114 D. Bi, A. M. El-Zohry, A. Hagfeldt and G. Boschloo, *ACS Appl. Mater. Interfaces*, 2014, **6**, 18751–18757.
115 H. Huang, J. Shi, L. Zhu, D. Li, Y. Luo and Q. Meng, *Nano Energy*, 2016, **27**, 352–358.
116 Q. Jiang, L. Zhang, H. Wang, X. Yang, J. Meng, H. Liu, Z. Yin, J. Wu, X. Zhang and J. You, *Nat. Energy*, 2016, **1**, 16177.
117 W. S. Yang, B. W. Park, E. H. Jung, N. J. Jeon, Y. C. Kim, D. U. Lee, S. S. Shin, J. Seo, E. K. Kim, J. H. Noh and S. I. Seok, *Science*, 2017, **356**, 1376–1379.
118 S. Yang, Y. C. Zheng, Y. Hou, X. Chen, Y. Chen, Y. Wang, H. Zhao and H. G. Yang, *Chem. Mater.*, 2014, **26**, 6705–6710.
119 Y. Fu, F. Meng, M. B. Rowley, B. J. Thompson, M. J. Shearer, D. Ma, R. J. Hamers, J. C. Wright and S. Jin, *J. Am. Chem. Soc.*, 2015, **137**, 5810–5818.
120 S. Rahimnejad, A. Kovalenko, S. M. Forés, C. Aranda and A. Guerrero, *ChemPhysChem*, 2016, **17**, 2795–2798.
121 H. Zhang, J. Mao, H. He, D. Zhang, H. L. Zhu, F. Xie, K. S. Wong, M. Grätzel and W. C. H. Choy, *Adv. Energy Mater.*, 2015, **5**, 1501354.
122 H.-S. Ko, J.-W. Lee and N.-G. Park, *J. Mater. Chem. A*, 2015, **3**, 8808–8815.
123 M. I. El-Henawey, R. S. Gebhardt, M. M. El-Tonsy and S. Chaudhary, *J. Mater. Chem. A*, 2016, **4**, 1947–1952.
124 C. Yi, X. Li, J. Luo, S. M. Zakeeruddin and M. Gratzel, *Adv. Mater.*, 2016, **28**, 2964–2970.
125 Y. Wu, A. Islam, X. Yang, C. Qin, J. Liu, K. Zhang, W. Peng and L. Han, *Energy Environ. Sci.*, 2014, **7**, 2934–2938.
126 W. S. Yang, J. H. Noh, N. J. Jeon, Y. C. Kim, S. Ryu, J. Seo and S. I. Seok, *Science*, 2015, **348**, 1234–1237.
127 Y. Zong, Y. Zhou, M. Ju, H. F. Garces, A. R. Krause, F. Ji, G. Cui, X. C. Zeng, N. P. Padture and S. Pang, *Angew. Chem., Int. Ed.*, 2016, **55**, 14723–14727.
128 G. Xu, R. Xue, W. Chen, J. Zhang, M. Zhang, H. Chen, C. Cui, H. Li, Y. Li and Y. Li, *Adv. Energy Mater.*, 2018, 1703054.
129 B. Li, J. Tian, L. Guo, C. Fei, T. Shen, X. Qu and G. Cao, *ACS Appl. Mater. Interfaces*, 2016, **8**, 4684–4690.
130 F. Ye, H. Chen, F. Xie, W. Tang, M. Yin, J. He, E. Bi, Y. Wang, X. Yang and L. Han, *Energy Environ. Sci.*, 2016, **9**, 2295–2301.
131 F. Ye, W. Tang, F. Xie, M. Yin, J. He, Y. Wang, H. Chen, Y. Qiang, X. Yang and L. Han, *Adv. Mater.*, 2017, **29**, 1701440.
132 H. Chen, F. Ye, W. Tang, J. He, M. Yin, Y. Wang, F. Xie, E. Bi, X. Yang, M. Gratzel and L. Han, *Nature*, 2017, **550**, 92–95.
133 A. Mei, X. Li, L. Liu, Z. Ku, T. Liu, Y. Rong, M. Xu, M. Hu, J. Chen, Y. Yang, M. Gratzel and H. Han, *Science*, 2014, **345**, 295–298.

134 Y. Hu, S. Si, A. Mei, Y. Rong, H. Liu, X. Li and H. Han, *Solar RRL*, 2017, **1**, 1600019.
135 T. Makris, A. Mourtzikou, A. Rapsomanikis and E. Stathatos, *Printable Sol. Cells*, 2017, 363–381.
136 X. Peng, J. Yuan, S. Shen, M. Gao, A. S. Chesman, H. Yin, J. Cheng, Q. Zhang and D. Angmo, *Adv. Funct. Mater.*, 2017, **27**, 1703704.
137 Z. Wei, H. Chen, K. Yan and S. Yang, *Angew. Chem., Int. Ed.*, 2014, **53**, 13239–13243.
138 F. Mathies, T. Abzieher, A. Hochstuhl, K. Glaser, A. Colsmann, U. W. Paetzold, G. Hernandez-Sosa, U. Lemmer and A. Quintilla, *J. Mater. Chem. A*, 2016, **4**, 19207–19213.
139 J. Tian, R. Gao, Q. Zhang, S. Zhang, Y. Li, J. Lan, X. Qu and G. Cao, *J. Phys. Chem. C*, 2012, **116**, 18655–18662.
140 D. Chen, F. Huang, Y. B. Cheng and R. A. Caruso, *Adv. Mater.*, 2009, **21**, 2206–2210.
141 S. Tang, Y. Deng, X. Zheng, Y. Bai, Y. Fang, Q. Dong, H. Wei and J. Huang, *Adv. Energy Mater.*, 2017, **7**, 1700302.
142 J. Li, R. Munir, Y. Fan, T. Niu, Y. Liu, Y. Zhong, Z. Yang, Y. Tian, B. Liu and J. Sun, *Joule*, 2018, **2**, 1313–1330.
143 Z. Bi, X. Rodríguez-Martínez, C. Aranda, E. Pascual-San-José, A. R. Goñi, M. Campoy-Quiles, X. Xu and A. Guerrero, *J. Mater. Chem. A*, 2018, **6**, 19085–19093.
144 M. He, B. Li, X. Cui, B. Jiang, Y. He, Y. Chen, D. O'Neil, P. Szymanski, M. A. Ei-Sayed, J. Huang and Z. Lin, *Nat. Commun.*, 2017, **8**, 16045.
145 Y. Deng, X. Zheng, Y. Bai, Q. Wang, J. Zhao and J. Huang, *Nat. Energy*, 2018, **3**, 560–566.
146 L. Mao, B. Luo, L. Sun, S. Xiong, J. Fan, F. Qin, L. Hu, Y. Jiang, Z. Li and Y. Zhou, *Mater. Horiz.*, 2018, **5**, 123–130.
147 J.-W. Lee, S.-I. Na and S.-S. Kim, *J. Power Sources*, 2017, **339**, 33–40.
148 F. C. Krebs, *Sol. Energy Mater. Sol. Cells*, 2009, **93**, 394–412.
149 E. Irissou, J.-G. Legoux, B. Arsenault and C. Moreau, *J. Therm. Spray Technol.*, 2007, **16**, 661–668.
150 C. Girotto, B. P. Rand, J. Genoe and P. Heremans, *Sol. Energy Mater. Sol. Cells*, 2009, **93**, 454–458.
151 G. Susanna, L. Salamandra, T. M. Brown, A. Di Carlo, F. Brunetti and A. Reale, *Sol. Energy Mater. Sol. Cells*, 2011, **95**, 1775–1778.
152 A. I. Martínez, D. R. Acosta and A. A. López, *J. Phys.: Condens. Matter*, 2004, **16**, S2335–S2344.
153 N. Lehraki, M. S. Aida, S. Abed, N. Attaf, A. Attaf and M. Poulain, *Curr. Appl. Phys.*, 2012, **12**, 1283–1287.
154 T. Wang, N. W. Scarratt, H. Yi, A. D. Dunbar, A. J. Pearson, D. C. Watters, T. S. Glen, A. C. Brook, J. Kingsley and A. R. Buckley, *Adv. Energy Mater.*, 2013, **3**, 505–512.
155 Y. S. Jung, K. Hwang, Y. J. Heo, J. E. Kim, D. Vak and D. Y. Kim, *Adv. Opt. Mater.*, 2018, **6**, 1701182.
156 J. E. Bishop, T. J. Routledge and D. G. Lidzey, *J. Phys. Chem. Lett.*, 2018, **9**, 1977–1984.
157 S. Das, B. Yang, G. Gu, P. C. Joshi, I. N. Ivanov, C. M. Rouleau, T. Aytug, D. B. Geohegan and K. Xiao, *ACS Photonics*, 2015, **2**, 680–686.
158 A. T. Barrows, A. J. Pearson, C. K. Kwak, A. D. F. Dunbar, A. R. Buckley and D. G. Lidzey, *Energy Environ. Sci.*, 2014, **7**, 2944–2950.
159 H. Ishihara, S. Sarang, Y.-C. Chen, O. Lin, P. Phummirat, L. Thung, J. Hernandez, S. Ghosh and V. Tung, *J. Mater. Chem. A*, 2016, **4**, 6989–6997.
160 C. Girotto, D. Moia, B. P. Rand and P. Heremans, *Adv. Funct. Mater.*, 2011, **21**, 64–72.
161 X. Fanton and A. Cazabat, *Langmuir*, 1998, **14**, 2554–2561.
162 J. H. Heo, M. H. Lee, M. H. Jang and S. H. Im, *J. Mater. Chem. A*, 2016, **4**, 17636–17642.
163 M. Habibi, A. Rahimzadeh, I. Bennouna and M. Eslamian, *Coatings*, 2017, **7**, 42.
164 F. C. Krebs, *Sol. Energy Mater. Sol. Cells*, 2009, **93**, 465–475.
165 A. Sandström, H. F. Dam, F. C. Krebs and L. Edman, *Nat. Commun.*, 2012, **3**, 1002.
166 L. Cai, L. Liang, J. Wu, B. Ding, L. Gao and B. Fan, *J. Semicond.*, 2017, **38**, 014006.
167 F. Di Giacomo, S. Shanmugam, H. Fledderus, B. J. Bruijnaers, W. J. H. Verhees, M. S. Dorenkamper, S. C. Veenstra, W. Qiu, R. Gehlhaar, T. Merckx, T. Aernouts, R. Andriessen and Y. Galagan, *Sol. Energy Mater. Sol. Cells*, 2018, **181**, 53–59.
168 T. Bu, S. Shi, J. Li, Y. Liu, J. Shi, L. Chen, X. Liu, J. Qiu, Z. Ku and Y. Peng, *ACS Appl. Mater. Interfaces*, 2018, **10**, 14922–14929.
169 Y. Hu, S. Si, A. Mei, Y. Rong, H. Liu, X. Li and H. Han, *Solar RRL*, 2017, **1**, 1600019.
170 H. Chen, F. Ye, W. Tang, J. He, M. Yin, Y. Wang, F. Xie, E. Bi, X. Yang and M. Grätzel, *Nature*, 2017, **550**, 92–95.
171 D. K. Mohamad, J. Griffin, C. Bracher, A. T. Barrows and D. G. Lidzey, *Adv. Energy Mater.*, 2016, **6**, 1600994.
172 X. Chen, H. Cao, H. Yu, H. Zhu, H. Zhou, L. Yang and S. Yin, *J. Mater. Chem. A*, 2016, **4**, 9124–9132.
173 B. Ding, L. Gao, L. Liang, Q. Chu, X. Song, Y. Li, G. Yang, B. Fan, M. Wang, C. Li and C. Li, *ACS Appl. Mater. Interfaces*, 2016, **8**, 20067–20073.
174 W. Chen, Y. Wu, Y. Yue, J. Liu, W. Zhang, X. Yang, H. Chen, E. Bi, I. Ashraful and M. Grätzel, *Science*, 2015, **350**, 944–948.
175 C. Liang, P. Li, H. Gu, Y. Zhang, F. Li, Y. Song, G. Shao, N. Mathews and G. Xing, *Solar RRL*, 2018, **2**, 1700217.
176 J. Lee, H. Kang, G. Kim, H. Back, J. Kim, S. Hong, B. Park, E. Lee and K. Lee, *Adv. Mater.*, 2017, **29**, 1606363.
177 M. Kim, G.-H. Kim, K. S. Oh, Y. Jo, H. Yoon, K.-H. Kim, H. Lee, J. Y. Kim and D. S. Kim, *ACS Nano*, 2017, **11**, 6057–6064.
178 Q. Jiang, Z. Chu, P. Wang, X. Yang, H. Liu, Y. Wang, Z. Yin, J. Wu, X. Zhang and J. You, *Adv. Mater.*, 2017, **29**, 1703852.
179 W. Qiu, T. Merckx, M. Jaysankar, C. Masse de la Huerta, L. Rakocevic, W. Zhang, U. W. Paetzold, R. Gehlhaar, L. Froyen, J. Poortmans, D. Cheyns, H. J. Snaith and P. Heremans, *Energy Environ. Sci.*, 2016, **9**, 484–489.
180 Y. Tu, J. Wu, X. He, P. Guo, T. Wu, H. Luo, Q. Liu, Q. Wu, J. Lin and M. Huang, *J. Mater. Chem. A*, 2017, **5**, 21161–21168.

181 H. Tan, A. Jain, O. Voznyy, X. Lan, F. P. Garcia de Arquer, J. Z. Fan, R. Quintero-Bermudez, M. Yuan, B. Zhang, Y. Zhao, F. Fan, P. Li, L. N. Quan, Y. Zhao, Z. H. Lu, Z. Yang, S. Hoogland and E. H. Sargent, *Science*, 2017, **355**, 722–726.
182 Y. Wu, X. Yang, W. Chen, Y. Yue, M. Cai, F. Xie, E. Bi, A. Islam and L. Han, *Nat. Energy*, 2016, **1**, 16148.
183 S. Cacovich, L. Ciná, F. Matteocci, G. Divitini, P. Midgley, A. Di Carlo and C. Ducati, *Nanoscale*, 2017, **9**, 4700–4706.
184 C.-Y. Chang, Y.-C. Chang, W.-K. Huang, W.-C. Liao, H. Wang, C. Yeh, B.-C. Tsai, Y.-C. Huang and C.-S. Tsao, *J. Mater. Chem. A*, 2016, **4**, 7903–7913.
185 K. Yao, X. Wang, Y.-x. Xu, F. Li and L. Zhou, *Chem. Mater.*, 2016, **28**, 3131–3138.
186 J. Seo, S. Park, Y. C. Kim, N. J. Jeon, J. H. Noh, S. C. Yoon and S. I. Seok, *Energy Environ. Sci.*, 2014, **7**, 2642–2646.
187 J. H. Heo, H. J. Han, D. Kim, T. K. Ahn and S. H. Im, *Energy Environ. Sci.*, 2015, **8**, 1602–1608.
188 K. Domanski, E. A. Alharbi, A. Hagfeldt, M. Grätzel and W. Tress, *Nat. Energy*, 2018, **3**, 61–67.
189 J. Yang, B. D. Siempelkamp, D. Liu and T. L. Kelly, *ACS Nano*, 2015, **9**, 1955–1963.
190 H. Tsai, R. Asadpour, J.-C. Blancon, C. C. Stoumpos, O. Durand, J. W. Strzalka, B. Chen, R. Verduzco, P. M. Ajayan and S. Tretiak, *Science*, 2018, **360**, 67–70.
191 R. Cheacharoen, N. Rolston, D. Harwood, K. A. Bush, R. H. Dauskardt and M. D. McGehee, *Energy Environ. Sci.*, 2018, **11**, 144–150.
192 M. Jung, T. J. Shin, J. Seo, G. Kim and S. I. Seok, *Energy Environ. Sci.*, 2018, **11**, 2188–2197.
193 Z. Wang, Q. Lin, F. P. Chmiel, N. Sakai, L. M. Herz and H. J. Snaith, *Nat. Energy*, 2017, **2**, 17135.
194 Y. I. Lee, N. J. Jeon, B. J. Kim, H. Shim, T.-Y. Yang, S. I. Seok, J. Seo and S. G. Im, *Adv. Energy Mater.*, 2018, **8**, 1701928.
195 G. E. Eperon, S. D. Stranks, C. Menelaou, M. B. Johnston, L. M. Herz and H. J. Snaith, *Energy Environ. Sci.*, 2014, **7**, 982–988.
196 T. Leijtens, K. Bush, R. Cheacharoen, R. Beal, A. Bowring and M. D. McGehee, *J. Mater. Chem. A*, 2017, **5**, 11483–11500.
197 M. Saliba, T. Matsui, J.-Y. Seo, K. Domanski, J.-P. Correa-Baena, M. K. Nazeeruddin, S. M. Zakeeruddin, W. Tress, A. Abate, A. Hagfeldt and M. Grätzel, *Energy Environ. Sci.*, 2016, **9**, 1989–1997.
198 D. P. McMeekin, G. Sadoughi, W. Rehman, G. E. Eperon, M. Saliba, M. T. Hörantner, A. Haghighirad, N. Sakai, L. Korte and B. Rech, *Science*, 2016, **351**, 151–155.
199 R. J. Sutton, G. E. Eperon, L. Miranda, E. S. Parrott, B. A. Kamino, J. B. Patel, M. T. Hörantner, M. B. Johnston, A. A. Haghighirad, D. T. Moore and H. J. Snaith, *Adv. Energy Mater.*, 2016, **6**, 1502458.
200 H. Bian, D. Bai, Z. Jin, K. Wang, L. Liang, H. Wang, J. Zhang, Q. Wang and S. F. Liu, *Joule*, 2018, **2**, 1500–1510.
201 S. Wang, C. Bi, J. Yuan, L. Zhang and J. Tian, *ACS Energy Lett.*, 2018, **3**, 245–251.
202 S. Ma, M. Cai, T. Cheng, X. Ding, X. Shi, A. Alsaedi, T. Hayat, Y. Ding, Z. a. Tan and S. Dai, *Sci. China Mater.*, 2018, **61**, 1257–1277.
203 Y. Lin, Y. Bai, Y. Fang, Z. Chen, S. Yang, X. Zheng, S. Tang, Y. Liu, J. Zhao and J. Huang, *J. Phys. Chem. Lett.*, 2018, **9**, 654–658.
204 L. Etgar, *Energy Environ. Sci.*, 2018, **11**, 234–242.
205 H. Tsai, W. Nie, J.-C. Blancon, C. C. Stoumpos, R. Asadpour, B. Harutyunyan, A. J. Neukirch, R. Verduzco, J. J. Crochet and S. Tretiak, *Nature*, 2016, **536**, 312–316.
206 W. Fu, J. Wang, L. Zuo, K. Gao, F. Liu, D. S. Ginger and A. K. Y. Jen, *ACS Energy Lett.*, 2018, **3**, 2086–2093.
207 T. Liu, Y. Zhou, Z. Li, L. Zhang, M. G. Ju, D. Luo, Y. Yang, M. Yang, D. H. Kim and W. Yang, *Adv. Energy Mater.*, 2018, 1800232.
208 C. Qin, T. Matsushima, T. Fujihara and C. Adachi, *Adv. Mater.*, 2016, **29**, 1603808.
209 Q. Wang, Q. Dong, T. Li, A. Gruverman and J. Huang, *Adv. Mater.*, 2016, **28**, 6734–6739.
210 X. Li, Z. Xue, D. Luo, C. Huang, L. Liu, X. Qiao, C. Liu, Q. Song, C. Yan, Y. Li and T. Wang, *Sci. China Mater.*, 2018, **61**, 363–370.
211 B. Li, C. Fei, K. Zheng, X. Qu, T. Pullerits, G. Cao and J. Tian, *J. Mater. Chem. A*, 2016, **4**, 17018–17024.
212 Y. Yue, N. Salim, Y. Wu, X. Yang, A. Islam, W. Chen, J. Liu, E. Bi, F. Xie and M. Cai, *Adv. Mater.*, 2016, **28**, 10738–10743.
213 Z. Wu and B. Sun, *Sci. China Mater.*, 2017, **61**, 125–126.
214 J. You, L. Meng, T. B. Song, T. F. Guo, Y. M. Yang, W. H. Chang, Z. Hong, H. Chen, H. Zhou, Q. Chen, Y. Liu, N. De Marco and Y. Yang, *Nat. Nanotechnol.*, 2016, **11**, 75–81.
215 T. Leijtens, G. E. Eperon, S. Pathak, A. Abate, M. M. Lee and H. J. Snaith, *Nat. Commun.*, 2013, **4**, 2885.
216 K. Domanski, J.-P. Correa-Baena, N. Mine, M. K. Nazeeruddin, A. Abate, M. Saliba, W. Tress, A. Hagfeldt and M. Grätzel, *ACS Nano*, 2016, **10**, 6306–6314.
217 Y. Kato, L. K. Ono, M. V. Lee, S. Wang, S. R. Raga and Y. Qi, *Adv. Mater. Int.*, 2015, **2**, 1500195.
218 Y. Deng, Q. Dong, C. Bi, Y. Yuan and J. Huang, *Adv. Energy Mater.*, 2016, **6**, 1600372.
219 F. Zhang, X. Yang, M. Cheng, W. Wang and L. Sun, *Nano Energy*, 2016, **20**, 108–116.
220 C.-H. Chiang, M. K. Nazeeruddin, M. Grätzel and C.-G. Wu, *Energy Environ. Sci.*, 2017, **10**, 808–817.
221 T. Singh and T. Miyasaka, *Adv. Energy Mater.*, 2018, **8**, 1700677.
222 N. Espinosa, L. Serrano-Luján, A. Urbina and F. C. Krebs, *Sol. Energy Mater. Sol. Cells*, 2015, **137**, 303–310.
223 F. Li and M. Liu, *J. Mater. Chem. A*, 2017, **5**, 15447–15459.
224 J. A. Christians, P. A. Miranda Herrera and P. V. Kamat, *J. Am. Chem. Soc.*, 2015, **137**, 1530–1538.
225 A. Babayigit, D. D. Thanh, A. Ethirajan, J. Manca, M. Muller, H.-G. Boyen and B. Conings, *Sci. Rep.*, 2016, **6**, 18721.
226 M. Lyu, J. H. Yun, P. Chen, M. Hao and L. Wang, *Adv. Energy Mater.*, 2017, **7**, 1602512.

227 M. Scholz, O. Flender, K. Oum and T. Lenzer, *J. Phys. Chem. C*, 2017, **121**, 12110–12116.
228 B. W. Park, B. Philippe, X. Zhang, H. Rensmo, G. Boschloo and E. M. Johansson, *Adv. Mater.*, 2015, **27**, 6806–6813.
229 W. Liao, D. Zhao, Y. Yu, C. R. Grice, C. Wang, A. J. Cimaroli, P. Schulz, W. Meng, K. Zhu and R. G. Xiong, *Adv. Mater.*, 2016, **28**, 9333–9340.
230 B. Saparov, F. Hong, J.-P. Sun, H.-S. Duan, W. Meng, S. Cameron, I. G. Hill, Y. Yan and D. B. Mitzi, *Chem. Mater.*, 2015, **27**, 5622–5632.
231 A. M. Elseman, A. E. Shalan, S. Sajid, M. M. Rashad, A. M. Hassan and M. Li, *ACS Appl. Mater. Interfaces*, 2018, **10**, 11699–11707.
232 N. K. Noel, S. D. Stranks, A. Abate, C. Wehrenfennig, S. Guarnera, A.-A. Haghighirad, A. Sadhanala, G. E. Eperon, S. K. Pathak and M. B. Johnston, *Energy Environ. Sci.*, 2014, **7**, 3061–3068.
233 H. Hu, B. Dong and W. Zhang, *J. Mater. Chem. A*, 2017, **5**, 11436–11449.
234 S. J. Lee, S. S. Shin, Y. C. Kim, D. Kim, T. K. Ahn, J. H. Noh, J. Seo and S. I. Seok, *J. Am. Chem. Soc.*, 2016, **138**, 3974–3977.
235 S. Shao, J. Liu, G. Portale, H.-H. Fang, G. R. Blake, G. H. ten Brink, L. J. A. Koster and M. A. Loi, *Adv. Energy Mater.*, 2018, **8**, 1702019.
236 C. Zuo and L. Ding, *Angew. Chem.*, 2017, **129**, 6628–6632.
237 F. Jiang, D. Yang, Y. Jiang, T. Liu, X. Zhao, Y. Ming, B. Luo, F. Qin, J. Fan, H. Han, L. Zhang and Y. Zhou, *J. Am. Chem. Soc.*, 2018, **140**, 1019–1027.
238 S. Paek, N. Cho, H. Choi, H. Jeong, J. S. Lim, J.-Y. Hwang, J. K. Lee and J. Ko, *J. Phys. Chem. C*, 2014, **118**, 25899–25905.
239 N.-G. Park, M. Grätzel, T. Miyasaka, K. Zhu and K. Emery, *Nat. Energy*, 2016, **1**, 16152.
240 M. Cai, Y. Wu, H. Chen, X. Yang, Y. Qiang and L. Han, *Adv. Sci.*, 2017, **4**, 1600269.
241 N. L. Chang, A. W. Yi Ho-Baillie, P. A. Basore, T. L. Young, R. Evans and R. J. Egan, *Prog. Photovolt.: Res. Appl.*, 2017, **25**, 390–405.
242 Z. Song, C. L. McElvany, A. B. Phillips, I. Celik, P. W. Krantz, S. C. Watthage, G. K. Liyanage, D. Apul and M. J. Heben, *Energy Environ. Sci.*, 2017, **10**, 1297–1305.
243 N. L. Chang, A. W. Y. Ho-Baillie, D. Vak, M. Gao, M. A. Green and R. J. Egan, *Sol. Energy Mater. Sol. Cells*, 2018, **174**, 314–324.